



**University of
Zurich**^{UZH}

**Zurich Open Repository and
Archive**

University of Zurich
University Library
Strickhofstrasse 39
CH-8057 Zurich
www.zora.uzh.ch

Year: 2013

**Inside out and upside down: Tracing the assembly of a simulated disk galaxy using
mono-age stellar populations**

Bird, Jonathan C ; Kazantzidis, Stelios ; Weinberg, David H ; Guedes, Javiera ; Callegari, Simone ; Mayer, Lucio ;
Madau, Piero

DOI: <https://doi.org/10.1088/0004-637X/773/1/43>

Posted at the Zurich Open Repository and Archive, University of Zurich

ZORA URL: <https://doi.org/10.5167/uzh-90707>

Journal Article

Accepted Version

Originally published at:

Bird, Jonathan C; Kazantzidis, Stelios; Weinberg, David H; Guedes, Javiera; Callegari, Simone; Mayer, Lucio; Madau, Piero (2013). Inside out and upside down: Tracing the assembly of a simulated disk galaxy using mono-age stellar populations. *Astrophysical Journal*, 773(1):43.

DOI: <https://doi.org/10.1088/0004-637X/773/1/43>

INSIDE OUT AND UPSIDE DOWN: TRACING THE ASSEMBLY OF A SIMULATED DISK GALAXY USING MONO-AGE STELLAR POPULATIONS

JONATHAN C. BIRD^{1,2,3,8}, STELIOS KAZANTZIDIS^{1,2}, DAVID H. WEINBERG^{1,2},
JAVIERA GUEDES⁴, SIMONE CALLEGARI⁵, LUCIO MAYER⁶, & PIERO MADAU⁷

Draft version June 7, 2013

ABSTRACT

We analyze the present-day structure and assembly history of a high resolution hydrodynamic simulation of the formation of a Milky Way (MW)-like disk galaxy, from the “Eris” simulation suite, dissecting it into cohorts of stars formed at different epochs of cosmic history. At $z = 0$, stars with $t_{\text{form}} < 2$ Gyr mainly occupy the stellar spheroid, with the oldest (earliest forming) stars having more centrally concentrated profiles. The younger age cohorts populate disks of progressively longer radial scale length and shorter vertical scale height. At a given radius, the vertical density profiles and velocity dispersions of stars vary smoothly as a function of age, and the superposition of old, vertically-extended and young, vertically-compact cohorts gives rise to a double-exponential profile like that observed in the MW. Turning to formation history, we find that the trends of spatial structure and kinematics with stellar age are largely imprinted at birth, or immediately thereafter. Stars that form during the active merger phase at $z > 3$ are quickly scattered into rounded, kinematically hot configurations. The oldest disk cohorts form in structures that are radially compact and relatively thick, while subsequent cohorts form in progressively larger, thinner, colder configurations from gas with increasing levels of rotational support. The disk thus forms “inside-out” in a radial sense and “upside-down” in a vertical sense. Secular heating and radial migration influence the final state of each age cohort, but the changes they produce are small compared to the trends established at formation. The predicted correlations of stellar age with spatial and kinematic structure are in good qualitative agreement with the correlations observed for mono-abundance stellar populations in the MW.

1. INTRODUCTION

EGGEN, LYNDEN-BELL, and SANDAGE (1962; hereafter, ELS) presented one of the earliest theoretical accounts of Milky Way (MW) formation: stars formed during the gravitational contraction of a rotating gas cloud, with successive generations forming successively more flattened, rotationally supported populations. They argued that this picture could explain the observed correlation between orbital eccentricity and chemical composition. Subsequent analytic models have emphasized the dark matter (DM) halo’s role as primary potential well and baryon angular momentum as a governor of disk scale length, with SN-driven outflows having a major impact on baryonic mass (e.g., White & Rees 1978; Fall & Efstathiou 1980; White & Frenk 1991; Kauffmann et al. 1993; Cole et al. 1994; Mo et al. 1998). In the cold dark matter (CDM) scenario, hierarchical structure formation leads to complex assembly histories whose effects can only be fully assessed with numerical simulations, which have grown steadily in computational and physical sophistication (e.g., Katz 1992;

Navarro & Steinmetz 1997; Brook et al. 2012, to give just three snapshots of a voluminous field). In this paper, we analyze one of the highest resolution simulations ever run of a MW-like galaxy formed from cosmological initial conditions to investigate its detailed assembly history.

The physics governing the construction of each major galactic component is likely to be different. Mergers and cannibalism of dwarf satellites may play a major role in the formation of the stellar halo, perhaps accounting for most of its mass (Searle & Zinn 1978; Bullock et al. 2001; Bullock & Johnston 2005). The bulge could be the remnant of early mergers (e.g., Hopkins et al. 2010) or the result of internal processes such as bar and bending instabilities that heat the inner disk over the life of the galaxy (e.g., Debattista et al. 2004, 2005). Thin disk formation is likely driven by gas dissipation and angular momentum conservation as in the classic picture. However, bimodal distributions in vertical star counts (e.g., Gilmore & Reid 1983), kinematics (e.g., Bensby et al. 2003), and chemistry (e.g., Lee et al. 2011) in the solar neighborhood suggest a distinct thick disk. Many theories of its origin have been proposed. The thick disk may arise from the accretion of stars stripped from satellites (Abadi et al. 2003), from a satellite dynamically heating a pre-existing stellar disk (e.g., Kazantzidis et al. 2008; Villalobos & Helmi 2008; Kazantzidis et al. 2009), from a gas rich merger at early times (Brook et al. 2004), from a clumpy and turbulent ISM at high redshift (e.g. Bournaud et al. 2009), or from stars migrating outwards from the hot, inner disk (Schönrich & Binney 2009a; Loebman et al. 2011).

Classic chemical evolution models describe disk galaxy formation using an inside-out star formation and chemical enrichment history (e.g., Matteucci & Francois 1989). This approach is sensible; the inner disk is thought to assemble first and form stars faster because of the high den-

¹ Department of Astronomy, The Ohio State University, 140 West 18th Avenue, Columbus, OH 43210

² Center for Cosmology and Astro-Particle Physics, The Ohio State University, 191 West Woodruff Avenue, Columbus, OH 43210

³ Department of Physics and Astronomy, Vanderbilt University, 6301 Stevenson Center, Nashville, TN, 37235

⁴ Institute for Astronomy, ETH Zürich, Wolfgang-Pauli-Strasse 27, 8093 Zürich, Switzerland

⁵ Anthropology Institute and Museum, University of Zürich, Winterthurerstrasse 190, CH-8057 Zürich, Switzerland

⁶ Institute for Theoretical Physics, University of Zürich, Winterthurerstrasse 190, CH-8057 Zürich, Switzerland

⁷ Department of Astronomy & Astrophysics, University of California, 1156 High Street, Santa Cruz, CA 95064

⁸ VIDA Postdoctoral Fellow

sity of accreted gas in the center of the galaxy’s potential well. However, both theoretical and observational studies over the last decade have emphasized the potential role of radial migration as a mechanism to redistribute stars and diversify the distribution of stellar chemical composition as a function of radius (e.g., Sellwood & Binney 2002; Haywood 2008; Roškar et al. 2008a; Schönrich & Binney 2009a; Casagrande et al. 2011; Minchev et al. 2012b). Radial migration alleviates tension between models and observations of the local stellar metallicity distribution and super metal rich stars in the solar annulus (Schönrich & Binney 2009a); it also naturally reproduces both the vertical density profile of stars and the chemical bimodality of the thin and thick disk (Schönrich & Binney 2009a,b). Still, the contribution of radial migration to the dynamical evolution of the disk, specifically thick disk dynamics, is currently debated in the literature (e.g., Schönrich & Binney 2009b; Loebman et al. 2011; Minchev et al. 2012a; Roškar et al. 2012b).

In this paper, we dissect a galaxy simulated in a fully cosmological context into individual age cohorts of stars formed at different epochs. We study the present-day spatial structure and kinematics of these cohorts, as well as their assembly history and radial migration patterns. Our results are less directly comparable to observations than chemistry-based investigations, but the age cohorts are physically simpler than chemically-selected tracer populations and avoid the uncertainties associated with numerical chemical enrichment implementation (e.g., Shen et al. 2010). In this paper, age cohorts reveal the expected inside-out growth of the disk. The simulated galaxy’s formation can also be described as “upside-down” in the sense that old stars form in a relatively thick component, or are kinematically heated very quickly after their birth. Younger populations form in successively thinner disks. Stars radially migrate throughout the galaxy’s assembly, but migrators do not disrupt the general kinematics-age trends put into place by the “upside-down” construction. There is some overlap of our results with those of Brook et al. (2012), who study the buildup of a chemically-defined thin disk, thick disk, and halo in the solar annulus of a less massive simulated disk galaxy; we discuss a comparison with their work in Section 6.

Motivation for our study comes partly from analysis of the SDSS Sloan Extension for Galactic Understanding and Exploration (SEGUE) (Yanny et al. 2009) G dwarf sample by Bovy et al. (2012a,b,c). They dissect the sample into groups spanning narrow ranges of $[\text{Fe}/\text{H}]$ and $[\alpha/\text{Fe}]$ and discover that the physical configuration of each mono-abundance population is well described by a single exponential function in both the radial and vertical directions; specifically, more alpha-rich, iron-poor (old) populations have shorter scale lengths but larger scale heights than alpha-poor, iron-rich (young) populations (see their Figure 5). Bovy et al. (2012a) use this result to contend that the MW’s thick disk is not a distinct structural component, a possibility raised by the mixture models of Nemeč & Nemeč (1991, 1993). The mono-abundance populations also have simple, isothermal kinematics in the vertical direction (Bovy et al. 2012c). The assembly histories of the age-cohorts (Section 4) illustrate the simulation’s fully self-consistent galaxy formation scenario that culminates in galactic structure (Section 3) qualitatively similar to the mono-abundance description of the MW.

2. THE SIMULATION

The cosmological simulation employed in the present study is part of the “Eris” campaign (Guedes et al. 2011) of hydrodynamical simulations of the formation of Milky Way (MW)-sized disk galaxies. It was performed with the parallel, TreeSPH N -body code GASOLINE (Wadsley et al. 2004) in a *Wilkinson Microwave Anisotropy Probe* 3-year cosmology ($\Omega_M = 0.24$, $\Omega_\Lambda = 0.76$, $\Omega_b = 0.042$, $H_0 = 73 \text{ km s}^{-1} \text{ Mpc}^{-1}$, $n = 0.96$, $\sigma_8 = 0.76$; Spergel et al. 2007).

All simulation parameters are identical to those of Guedes et al. (2011), except for the star formation efficiency parameter, which was equal to $\epsilon_{\text{SF}} = 0.1$ in the latter study, but it is $\epsilon_{\text{SF}} = 0.05$ in the simulation employed here (see below). Specifically, we started from a low-resolution (300^3 particles), DM-only simulation corresponding to a periodic box of 90 Mpc on a side. The target halo was identified at $z = 0$ and was chosen to have a mass similar to that of the MW and a rather quiet late merging history, namely to have experienced no major mergers (defined as encounters with mass ratios $\geq 1/8$) after $z = 3$. Three halos with masses between 6×10^{11} and $8 \times 10^{11} M_\odot$ satisfied these conditions in the $(90 \text{ Mpc})^3$ box, and we chose to re-simulate the one which appeared to be most “regular” and isolated, with a virial mass of $M_{\text{vir}} = 7.9 \times 10^{11} M_\odot$ at $z = 0$.

New initial conditions were then generated with improved mass resolution (by a factor 20^3) on a nested grid in a Lagrangian sub-region of size 1 Mpc, centered around the chosen halo, using the standard “zoom-in” technique to add small-scale perturbations. High-resolution particles were further split into 13 million dark matter particles and an equal number of gas particles, for a final dark and gas particle mass of $m_{\text{DM}} = 9.8 \times 10^4 M_\odot$ and $m_{\text{SPH}} = 2 \times 10^4 M_\odot$, respectively. The gravitational softening length was fixed to 120 pc for all particle species from $z = 9$ to $z = 0$, and evolved as $1/(1+z)$ from $z = 9$ to the starting redshift of $z = 90$. At the present epoch, the simulation contains ~ 7 , ~ 3 , and ~ 8.6 million dark matter, gas, and star particles, respectively, for a total of $N \sim 18.6$ million particles within the virial radius ($R_{\text{vir}} \sim 239 \text{ kpc}$).

The version of GASOLINE used in this study includes Compton cooling, atomic cooling, and metallicity-dependent radiative cooling at low temperatures (Mashchenko et al. 2006). A uniform UV background modifies the ionization and excitation state of the gas and is implemented using a modified version of the Haardt & Madau (1996) spectrum.

Our star formation recipe follows that of Stinson et al. (2006), which is based on that of Katz (1992). Star formation occurs when cold ($T < T_{\text{max}}$), virialized gas that is part of a converging flow reaches a threshold density (n_{SF}). Gas particles spawn stellar particles with a given efficiency ϵ_{SF} at a rate proportional to the local dynamical time, t_{dyn} ,

$$d\rho_*/dt = \epsilon_{\text{SF}} \rho_{\text{gas}} / t_{\text{dyn}} \propto \rho_{\text{gas}}^{1.5} \quad (1)$$

(i.e., locally enforcing a Schmidt law), where ρ_* and ρ_{gas} are the stellar and gas densities, respectively. In our simulation, $T_{\text{max}} = 3 \times 10^4 \text{ K}$, $n_{\text{SF}} = 5 \text{ atoms cm}^{-3}$, and $\epsilon_{\text{SF}} = 0.05$.

Star particles are created stochastically with an initial mass $m_* \sim 6.2 \times 10^3 M_\odot$, and the gas particle that spawns the new star has its own mass reduced accordingly. Gas particles are deleted from the simulation once their masses fall below $\sim 4 \times 10^3 M_\odot$ (with their masses and metals being distributed in neighboring gas particles). A newly formed star particle represents a simple stellar population with its own age and

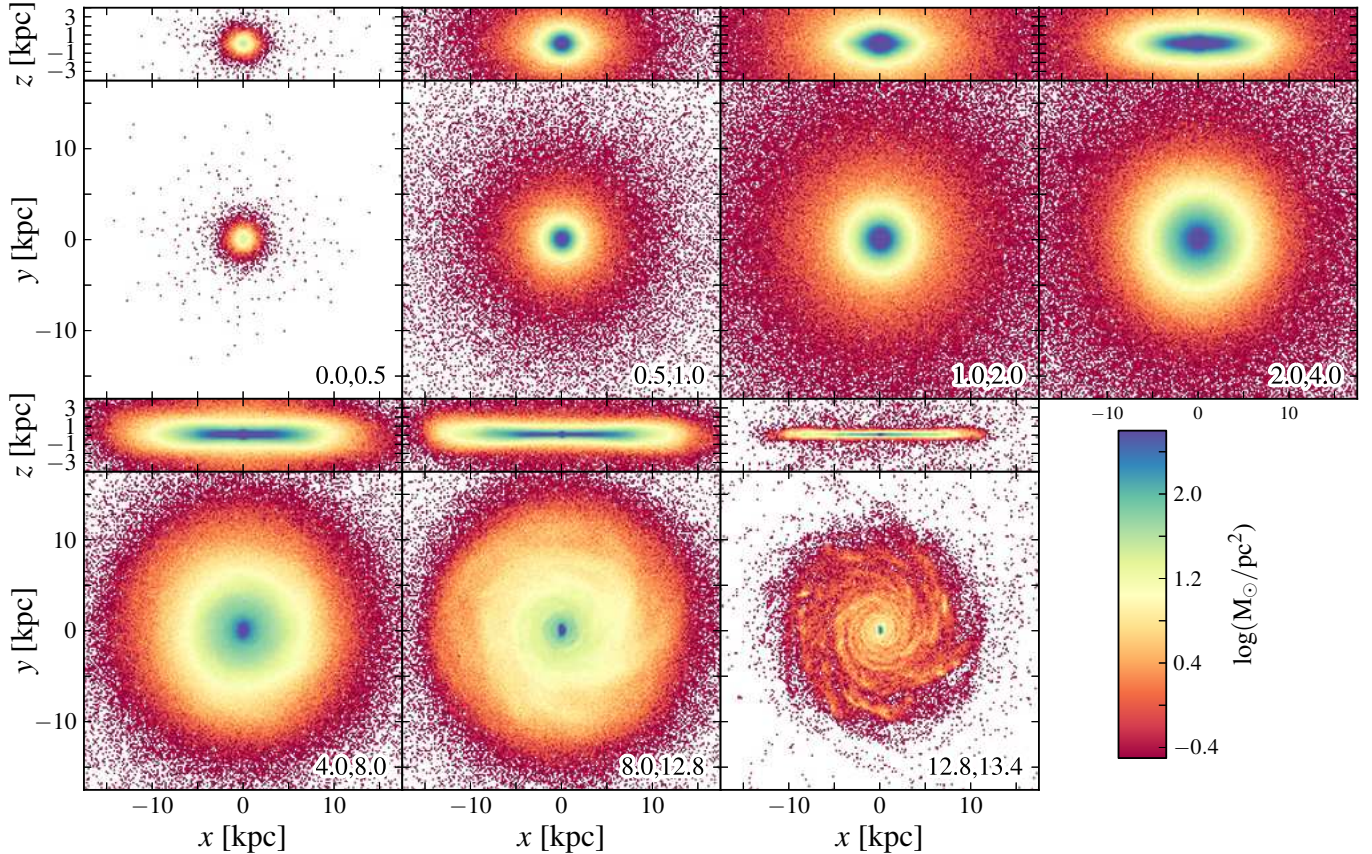


FIG. 1.— The present-day surface density of stars in the simulated galaxy as a function of position and age. Each panel shows the face-on and edge-on views of a single age cohort (formation time bins, in Gyr after the big bang, are denoted in the bottom right corner of each panel); pixel color represents the logarithmic surface density at the pixel position (see colorbar). The coordinate system is such that the disk lies in the xy plane and the galaxy’s angular momentum vector is aligned with the z axis. Age cohort spatial structure smoothly evolves: old populations are radially short and vertically extended; younger cohorts with later formation times inhabit progressively longer and thinner disks.

metallicity and a Kroupa et al. (1993) initial stellar mass function.

Feedback from supernovae (SNe) is treated using the blast-wave model described by Stinson et al. (2006), which is based on the analytic treatment of blastwaves described by McKee & Ostriker (1977). Each Type-II SN deposits metals and a net thermal energy of $\epsilon_{\text{SN}} \times 10^{51}$ ergs into the nearest neighboring gas particles, and the fraction of energy that couples to the interstellar medium was set to $\epsilon_{\text{SN}} = 0.8$ (the same value was adopted in previous cosmological simulations; see, for example, Governato et al. 2007). The heated gas has its cooling shut off for a timescale set by the local gas density and temperature and by the total amount of energy injected (Stinson et al. 2006). The energy deposited by many SNe adds up to create larger, hot bubbles and longer cooling shut-off times. No feedback from an active galactic nucleus was included in the simulation.

Our high mass and force resolution enables us to adopt a density threshold for star formation that is 50 times higher compared to those employed in previous lower-resolution studies. The local Jeans length corresponding to our density threshold and $T = 10^3 K$ is resolved with more than 5 SPH smoothing lengths, and thus artificial fragmentation is prevented (Bate & Burkert 1997); we note that very few gas particles inside the virial radius ever cool below $10^3 K$. Similarly, the Jeans mass at our threshold density is resolved with at least 100 m_{SPH} , where m_{SPH} denotes the mass of the SPH gas particle. Lastly, we stress that the star formation density thresh-

old adopted here is high enough to allow the development of a clumpy, inhomogeneous ISM, which serves as a vital element for the formation of realistic disk galaxies (Guedes et al. 2011).

Our simulation produces a galaxy that at $z=0$ has structural properties nearly identical to those of the base “Eris” run described by Guedes et al. (2011) (for example the bulge-to-disk ratio and the radial scale length of the disk differ by less than 10% in the two simulations; see Mayer 2012). Although we defer a detailed comparison of the two simulations to future work, we stress that the rotation curve of our resulting galaxy is even flatter than that of Guedes et al. (2011), perhaps because the nuclear bar is weaker and thus less dense, providing an even better match to the rotation curve of a typical late-type Sb/Sbc spiral galaxy.

3. THE PRESENT-DAY GALAXY

We denote stellar populations grouped by age (age cohorts) with a script \mathcal{S} and subscripts corresponding to the population’s range in formation time; e.g., stars born between 0.0 and 0.5 Gyr after the big bang will be collectively referred to as $\mathcal{S}_{0.0,0.5}$. Cohort age is the difference between the age of the universe in the simulation (13.327 Gyr) and the cohort’s formation time.

Figure 1 shows the stellar surface density of the galaxy as a function of position and age at redshift zero. The specific age cohorts are defined by formation times (t_{form}) spanning 0.0 to 0.5 Gyr, 0.5 to 1.0 Gyr, 1.0 to 2.0 Gyr, 2.0 to 4.0

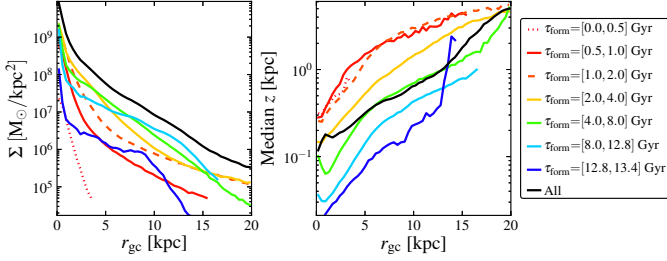


FIG. 2.— The radial profiles of surface mass density (left panel) and median height above the disk plane (right panel) for all age cohorts at redshift zero. Note r_{gc} , used throughout this paper, refers to galactocentric radius. The color of each radial profile indicates cohort formation time; colors progress from red for old stars to blue for young stars (see legend for details); in addition to color, line types help differentiate the oldest cohorts). We also plot the surface mass density and median height of all stars (thick, black lines). All radial profiles in this paper have 0.37 kpc bins; bins with $n < 10$ particles are left blank. Younger cohorts populate more disk-like configurations and reside closer to the plane than their older counterparts.

Gyr, 4.0 to 8.0 Gyr, 8.0 to 12.8 Gyr, and the final ~ 500 Myr of star formation, 12.8 to 13.4 Gyr⁹. Each panel denotes the range of t_{form} considered and shows face-on and edge-on views of the galaxy. Following the density distributions from left to right and top to bottom, younger stellar populations show longer, thinner structure than older populations. The oldest cohort ($\mathcal{S}_{0.0,0.5}$) is concentrated in the central region of the galaxy while stars born during the next 500 Myr ($\mathcal{S}_{0.5,1.0}$) have a spheroidal mass density profile out to a galactocentric radius (r_{gc}) of ~ 10 kpc. Compared to stars with $t_{\text{form}} < 1$ Gyr, $\mathcal{S}_{1.0,2.0}$ extends further in radius, and its edge-on view shows a distinct yet subdominant flattened component indicative of an infant disk. $\mathcal{S}_{2.0,4.0}$ is the first cohort to display primarily non-spheroidal spatial structure; the edge-on view shows a vertically extended and relatively compact disk. Edge-on views of $\mathcal{S}_{4.0,8.0}$ and $\mathcal{S}_{8.0,12.8}$ reveal that younger populations inhabit progressively longer and thinner disks. $\mathcal{S}_{12.8,13.4}$ is confined predominantly to the spiral arms and has a very sharp break at $r_{\text{gc}} \approx 10$ kpc (Figure 1, face-on view). In time, the $\mathcal{S}_{12.8,13.4}$ stars in these spiral arms will heat up and increase their random motions, eventually leading to the dissolution of the cohort’s present-day structure (though newly formed stars would enable the spiral arms to persist). The reduced azimuthal structure in the density distributions of $\mathcal{S}_{4.0,8.0}$ and $\mathcal{S}_{8.0,12.8}$ are suggestive of how the spiral overdensity can fade over time. As descriptions of galaxy morphology, the terms “early” and “late” have largely lost their evolutionary connotations, but it is intriguing that the configurations of the age cohorts within this individual simulated galaxy map almost perfectly onto the Hubble sequence from early-type elliptical to late-type spiral.

The age cohorts’ surface mass density profiles quantify their mass contribution to the galaxy as a function of radius (Figure 2, left panel). The color scheme for this figure is repeated throughout the rest of the paper: red colors for the oldest cohorts, progressing through orange, yellow, green, cyan, and dark blue for younger populations. A bulge-like component dominates the inner 2 kpc of the surface mass density profile for all stars (black line); starting at $r_{\text{gc}} \sim 3.5$ kpc, the profile becomes exponential and shows no break out to $r_{\text{gc}} = 20$ kpc. As seen in Figure 1, $\mathcal{S}_{0.0,0.5}$ contributes only to the central region of the galaxy. The mass density profiles of $\mathcal{S}_{0.5,1.0}$ and $\mathcal{S}_{1.0,2.0}$ extend to larger radii and are intermediate

⁹ The bin edge is at 13.4 Gyr as it is the nearest 100 Myr increment that was inclusive of all stars.

TABLE 1
KINEMATIC DECOMPOSITION

t_{form} (Gyr)	ID	f_{mass}	f_{thin}	f_{thick}	f_{pseudo}	f_{spheroid}
(0.0,0.5)	$\mathcal{S}_{0.0,0.5}$	0.002	0.018	0.010	0.223	0.749
(0.5,1.0)	$\mathcal{S}_{0.5,1.0}$	0.058	0.021	0.053	0.182	0.743
(1.0,2.0)	$\mathcal{S}_{1.0,2.0}$	0.186	0.103	0.111	0.250	0.536
(2.0,4.0)	$\mathcal{S}_{2.0,4.0}$	0.313	0.438	0.143	0.211	0.208
(4.0,8.0)	$\mathcal{S}_{4.0,8.0}$	0.260	0.725	0.045	0.097	0.134
(8.0,12.8)	$\mathcal{S}_{8.0,12.8}$	0.165	0.852	0.015	0.073	0.060
(12.8,13.4)	$\mathcal{S}_{12.8,13.4}$	0.017	0.907	0.023	0.051	0.018
Total		1.000	0.501	0.083	0.161	0.254

NOTE. — The fractional contribution of each age cohort to different galactic structures at redshift zero. The range of formation time, in Gyr, defining each age cohort is in Column 1. The textual representation of each cohort is in Column 2. The fraction of present-day stellar mass in the cohort is in Column 3. The fraction of each cohort assigned to the thin disk, thick disk, pseudobulge, and spheroid using our kinematic decomposition procedure (see text) is listed in Columns 4, 5, 6, and 7, respectively.

in shape between a power law and exponential characterization. In addition to a central power law distribution, $\mathcal{S}_{2.0,4.0}$ has a qualitatively exponential component at $3 < r_{\text{gc}} < 10$ kpc. Younger populations show dominant exponential components: the mass density profile of $\mathcal{S}_{4.0,8.0}$ is exponential at $3 < r_{\text{gc}} < 20$ kpc while that of $\mathcal{S}_{8.0,12.8}$ has two exponential components over the same radial range with a break at $r_{\text{gc}} \sim 12.5$ kpc. Stars born in the last 500 Myr have the mass profile of a exponential disk with a break radius at 9 kpc. The cohorts also show trends in their vertical structure: older populations are systematically at greater heights above the plane than younger cohorts at all galactocentric radii (right panel, Figure 2). Several groups have measured a similar correlation at the solar annulus in the MW and in external galaxies (e.g., Bensby et al. 2005; Yoachim & Dalcanton 2008). Note that the precipitous rise in the median height above the plane in $\mathcal{S}_{12.8,13.4}$ occurs past the break radius of this population; only a few percent of this cohort’s mass is found in the disk outskirts, and these stars may be kinematically distinct from those inside the break. The median height of all stars is correlated with r_{gc} , partly because of an increasing halo to disk ratio in the outskirts of the galaxy (see Section 6 for the same analysis applied to a kinematically selected disk sample).

We show each age cohort’s vertical density profile at three different galactocentric radii in Figure 3. The profile of all stars in the solar annulus ($7 < r_{\text{gc}} < 9$ kpc, middle panel, black line) is consistent with the classic two exponential profile shape observed in the MW (Gilmore & Reid 1983) and recently measured to have scale heights $z_{\text{thin}} = 0.3$ kpc and $z_{\text{thick}} = 0.9$ kpc (Jurić et al. 2008); the simulated galaxy’s scale heights are a factor of 1.6–1.8 larger at $z_{\text{thin}} = 0.55$ kpc and $z_{\text{thick}} = 1.47$ kpc but maintain the same thick to thin disk ratio. Traditionally, this double-exponential vertical density profile has been interpreted as two distinct structural components, but Figure 3 clearly shows that the superposition of all cohort vertical density profiles, spanning a continuum of scale heights (increasing with age), naturally yields the double-exponential profile (see Section 6). Incorporating data from the inner and outer disk (left and right panels, respectively), we find two general trends governing the relationship between age, scale height, and radius: older stellar populations have more extended vertical density profiles than younger age cohorts, while each individual cohort’s vertical profile becomes more extended at larger radii.

The galaxy has dynamical trends with age as well: the or-

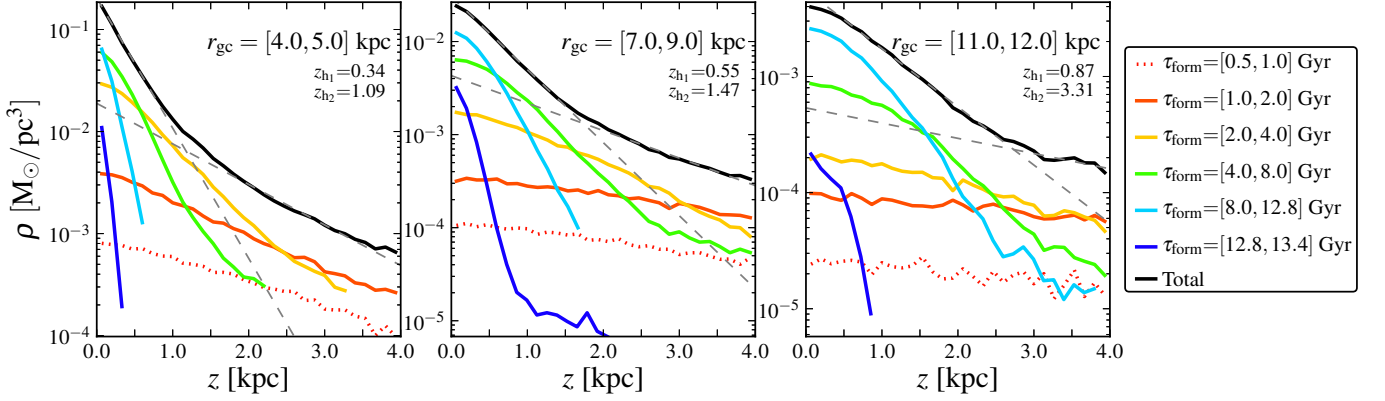


FIG. 3.— Vertical mass density profiles of the age cohorts at the three labeled radial annuli in the disk (from left to right: $r_{\text{gc}} = [4.0, 5.0]$, $[7.0, 9.0]$, and $[11.0, 12.0]$ kpc). The y axis for all panels is the mass density in $M_{\odot} \text{pc}^{-3}$. The x axis shows the same range in height above the plane (in kpc) for all panels. The color-coding is the same as in Figure 2 (see legend). Thick, black lines represent the total vertical mass density profile in each annulus. We fit two exponential profiles to the total mass density in each panel (gray, dashed lines); the scale height of each fit is listed in the upper right of each panel. Note that there is no significant $\mathcal{S}_{0,0,0.5}$ population at these annuli.

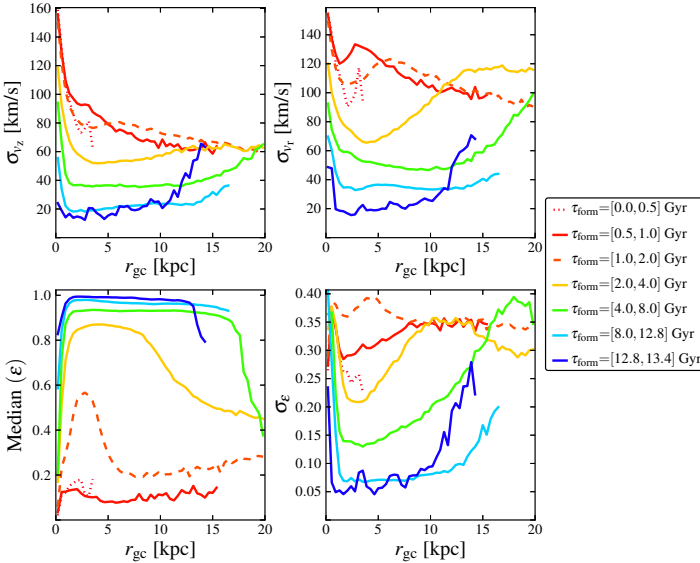


FIG. 4.— The present-day radial profiles of vertical velocity dispersion (top left), radial velocity dispersion (top right), median circularity (bottom left, $\epsilon = j_z/j_{\text{circ}}$, where j_z is a particle’s angular momentum and j_{circ} the angular momentum for a circular orbit with the particle’s energy E), and dispersion of circularity (bottom right) for each age cohort. Younger cohorts are kinematically colder than older cohorts. The color of each radial profile indicates the cohort age as in Figure 2 (see legend).

bits of older age cohorts are systematically hotter than their younger counterparts in the radial and vertical directions at nearly all radii (top row of Figure 4). The same general trend is seen in studies based on the Geneva Copenhagen Survey in the MW (Holmberg et al. 2007; Casagrande et al. 2011), though some explorations of smaller data sets find a plateau in the age-velocity relationship for stars of intermediate age (e.g., Wielen 1977; Quillen & Garnett 2001; Soubiran et al. 2008). Each individual age cohort’s velocity dispersion profiles have note-worthy features. The velocity dispersions of $\mathcal{S}_{0.5,1.0}$ and $\mathcal{S}_{1.0,2.0}$ are locally maximal at the edges of their bulge-like mass distributions ($r_{\text{gc}} \sim 3$ and 6 kpc, respectively). Each cohort of stars with $t_{\text{form}} > 4$ Gyr shows little internal variation in velocity dispersion as a function of radius in the galaxy’s disk out to $r_{\text{gc}} \sim 12.5$ kpc; thereafter, there is a positive gradient in σ_{v_r} and σ_{v_z} with radius. Interestingly, the mass density profile of $\mathcal{S}_{2.0,4.0}$ is consistent with that of an exponen-

tial disk at $r_{\text{gc}} > 5$ kpc (Figure 4), yet this radius is precisely the starting point for a large, positive radial gradient in its σ_{v_r} and (to a lesser degree) σ_{v_z} profiles, which is not seen in the younger cohorts except for the sparse outskirts of $\mathcal{S}_{12.8,13.4}$. It is plausible that the vertically extended disk of $\mathcal{S}_{2.0,4.0}$ experienced a significantly different evolutionary history than the younger disk populations.

The bottom row of Figure 4 examines the orbital shape (circularity) of cohort members as a function of radius. To define orbital circularity (ϵ), we first choose a coordinate system such that the origin is coincident with the stellar particles’ center of mass and the z -axis is aligned with the total angular momentum vector of the stars. Each particle’s angular momentum in the plane of the disk is then j_z , and positive j_z denotes a corotating orbit. Circular orbits have the maximal j_z (hereafter j_{circ}) given a particle’s total energy (E_{tot} , see below). A particle’s circularity (ϵ) is defined as $j_z/j_{\text{circ}}(E_{\text{tot}})$. Following the trends in velocity dispersion, older stars are on less circular orbits and show more variation in their orbital shape than younger populations. The median circularity within the disk components of $\mathcal{S}_{2.0,4.0}$, $\mathcal{S}_{4.0,8.0}$, and $\mathcal{S}_{8.0,12.8}$ remains constant over a radial range that increases when younger populations are considered. The dispersion in circularity, however, grows with radius for these three cohorts; the radial onset of the increase is inversely correlated with age. Stars formed during the last 500 Myr are generally born on very circular orbits and only have significant circularity dispersion past the $\mathcal{S}_{12.8,13.4}$ disk break radius.

To aid in our description of the current state of the galaxy, we kinematically separate the galaxy into structural components using particle energy and angular momentum and following a modified version of the prescription outlined in Abadi et al. (2003). We adhere to convention and describe these components as the “thin disk”, “pseudobulge”, etc., though this nomenclature implies, to some degree, sharp distinctions in the observed continuous distribution.

The principal discriminants in our decomposition are circularity and total specific energy defined by $E_{\text{tot}} = \frac{1}{2}v^2 + \Phi$; where v is the total velocity of the particle and Φ is the value of the potential (an output of the simulation code) at the position of the particle. We first assign all particles with $\epsilon > 0.8$ to the thin disk as it should contain mostly circular orbits ($\epsilon = 1$ for a circular orbit). We assign to the spheroid all particles with circularity below a critical threshold $\epsilon_{\text{crit}} = 0.33$, which is cho-

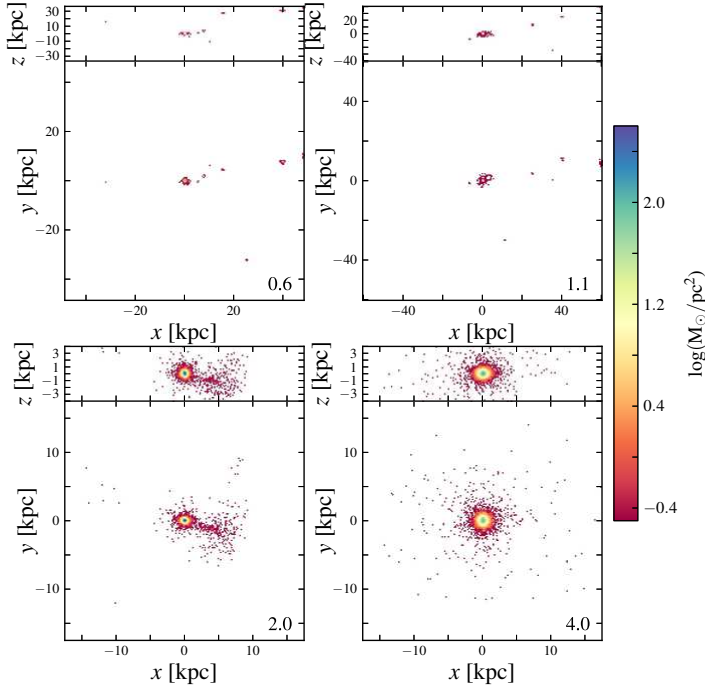


FIG. 5.— The surface density of $S_{0,0,0.5}$ as a function of position and time. Edge-on and face-on views are shown at the time of each snapshot (labeled in gigayears at the bottom right hand corner of each panel). Pixel color represents the logarithmic surface mass density at the pixel position (see colorbar). The coordinate system is such that the disk lies in the xy plane and the galaxy’s angular momentum vector is aligned with the z axis. Note the changing spatial scale: for clarity, our axis limits either correspond to the box encompassing 95% of the cohort’s mass or the region considered in Figure 1 ($(|x|, |y|, |z| < 17.5, 17.5, 4.0$ kpc), whichever is larger). $S_{0,0,0.5}$ assembles in the center of the galaxy quickly. Snapshots at later times show no qualitative differences with $t = 4.0$ Gyr.

sen such that the ensemble of all particles with $\epsilon < \epsilon_{\text{crit}}$ exhibit zero net rotation (all counter-rotating particles are assigned to the spheroid). The remaining population has $\epsilon_{\text{crit}} < \epsilon < 0.8$ and is subdivided into the thick disk ($E_{\text{tot}} \geq E_*$) and pseudobulge ($E_{\text{tot}} < E_*$) based on the median energy of all stellar particles (E_*). Note that this definition of pseudobulge is not identical to that used in Guedes et al. (2012), where the pseudobulge was first identified photometrically as the stellar mass contained in the inner 2 kpc, which has a higher Sec profile index than the disk. Their pseudobulge was then constrained further by including only stars with circularity below 0.8 to exclude disk stars. A fraction of stars that we identify as belonging to the thick disk via the energy cut or to the spheroid via the circularity threshold would have been classified as pseudobulge using the Guedes et al. (2012) definition.

Our kinematic distinctions are somewhat arbitrary and may not perfectly describe the galaxy. The caveats to this decomposition are similar to those in Abadi et al. (2003): the spheroidal component could have a modest amount of rotation in reality, the circularity cutoff for the thin disk may not precisely match that in the MW, and the energy cuts do not ensure that our structural distinctions are complete and free of contamination. In addition, our choice to uniquely assign all regions of the E_{tot}, ϵ plane to specific structures demands that the ϵ distribution of the spheroid is not symmetric about $\epsilon = 0$, extending to $\epsilon = -1$ for counter-rotating stars but stopping at ϵ_{crit} for co-rotating orbits. We stress that our subsequent analysis and conclusions are not based on these kinematic selections. However, the decomposition gives us a qualitative

description of the galaxy’s kinematic structure that provides a familiar context for our analysis.

In Table 1, we show how each age cohort contributes to the galactic structures identified in our kinematic decomposition. The results corroborate much of what we see in Figure 1. Old stellar populations with $t_{\text{form}} < 2.0$ Gyr predominantly contribute to the spheroid. After $t = 4$ Gyr, new stars overwhelmingly populate the disk of the galaxy. $S_{2,0,4,0}$ is an intermediate population: significant fractions of its members have kinematics consistent with classical disk and spheroid orbits. The total fractions confirm that the simulated galaxy has a strong disk component. The majority of all particles have high circularity ($f_{\epsilon > 0.7} = 0.6$), similarly prominent high circularity populations are found in the most disk-dominated galaxies simulated with the latest implementation of the TreeSPH code GADGET-3 (Aumer et al. 2013).

4. EVOLUTION OF AGE COHORTS

We now examine the assembly history of the galaxy using the individual age cohorts as tracer populations. In this section we adjust our choice of age cohorts so that each represents at most a 1 Gyr range of formation times. The first three t_{form} bins ($S_{0,0,0.5}$, $S_{0.5,1,0}$, and $S_{1,0,2,0}$) are illustrative of the relatively complex assembly of stellar populations at early times. $S_{3,0,4,0}$ is an “intermediate” population born just after the major merger epoch concludes. The final age cohort described here, $S_{7,0,8,0}$, is representative of populations born and evolved *in situ* in a quiescent disk.

The First 500 Myr We consider the surface density distribution of $S_{0,0,0.5}$ as a function of time, specifically at $t = 0.6, 1.1, 2.0,$ and 4.0 Gyr, in Figure 5. These stars populate a number of different subhalos at early times, but their dominant concentration is in the parent halo of the galaxy (note the changing scale on each panel in the figure). The final merger event involving a perceptible fraction of $S_{0,0,0.5}$ is well underway at $t = 2$ Gyr; by $t = 4$ Gyr, $S_{0,0,0.5}$ has assembled into a configuration much like what we see today (compare the bottom right of Figure 5 with the top left of Figure 1). We omit snapshots at later times as $S_{0,0,0.5}$ shows no further qualitative changes in its density distribution.

Physical parameters describing spatial structure and kinematics confirm that the $S_{0,0,0.5}$ population assembles fairly rapidly and evolves quiescently thereafter (Figure 6). Both the satellite accretion and the decreasing central density seen in Figure 5 broaden the cohort’s radial surface mass density profile with time. The radial profiles of vertical velocity dispersion (right panel) and median height above the plane (middle panel) show that $S_{0,0,0.5}$ kinematically heats up as it assembles but only makes moderate energy gains after $t = 4$ Gyr. $S_{0,0,0.5}$ congregates early in the galaxy’s history, remains centrally concentrated, and evolves quiescently after its last substantial merger event.

$t_{\text{form}} = [0.5, 1.0]$ Gyr Similar to $S_{0,0,0.5}$, $S_{0.5,1,0}$ is scattered amongst several subhalos at early times but most of its mass is still born in the parent halo (Figure 7). The merger event at $t = 2$ Gyr is more significant for $S_{0.5,1,0}$ than $S_{0,0,0.5}$. Still, after another 2 Gyr, the morphological features associated with the encounter have dissipated. From $t = 4$ Gyr to $t = 6$ Gyr, the density distribution of stars outside $r_{\text{gc}} > 6$ kpc becomes more symmetric. Later snapshots do not show any qualitative changes.

The surface mass density radial profile of $S_{0.5,1,0}$ resembles its current state throughout most of the galaxy by $t \sim 4$ Gyr; however, a perceptible decrease in mass within the innermost

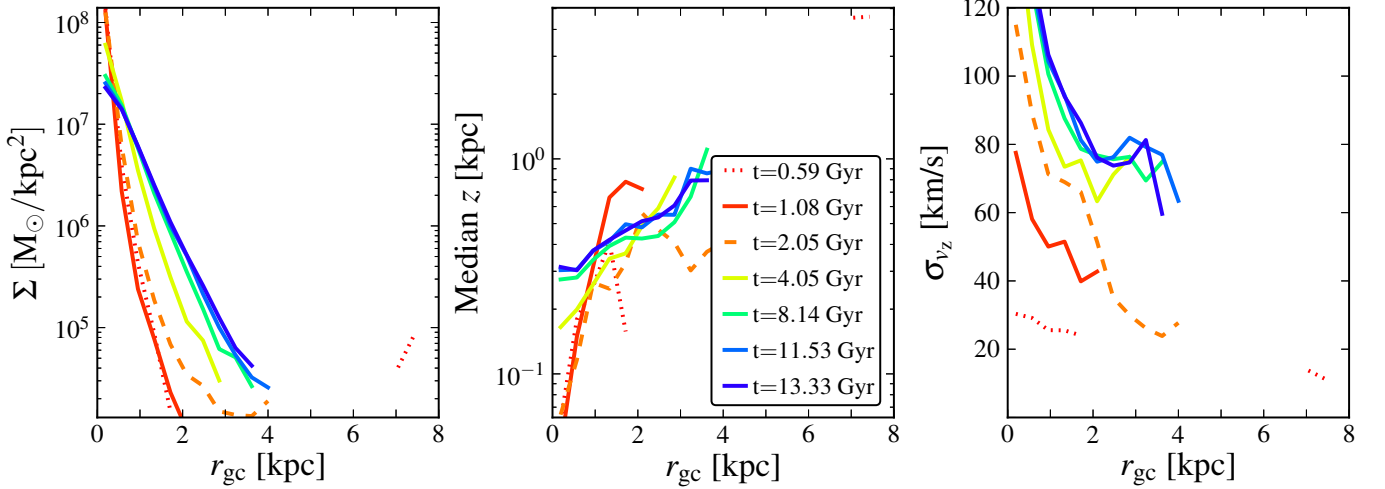


FIG. 6.— The radial profiles of surface mass density (left panel), median height above the disk plane (middle panel), and vertical velocity dispersion (right panel) for $S_{0,0,0.5}$ as a function of time. The color of each line represents the age of the simulation when the profile was measured (see legend in middle panel). Note that the colors progress from red for early times to blue for late times; we adopt this color scheme throughout the rest of the figures. Line types help differentiate the earliest outputs.

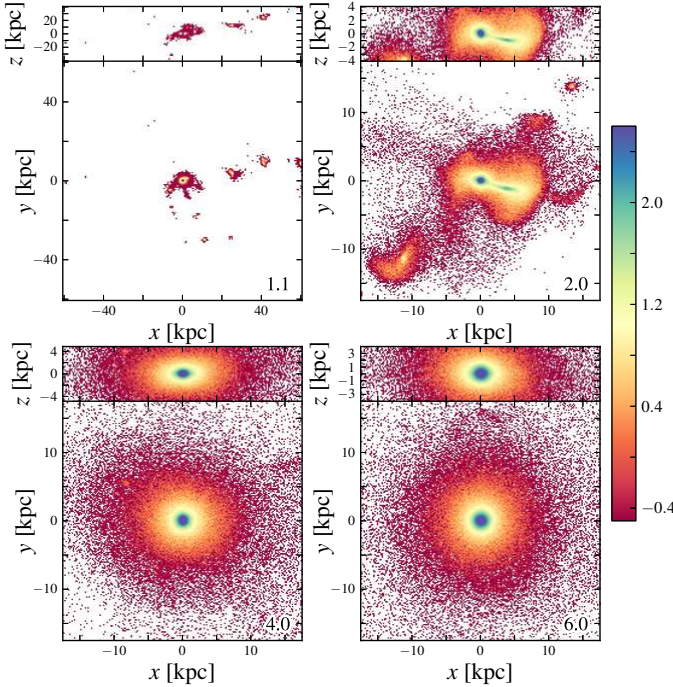


FIG. 7.— The surface density of $S_{0.5,1,0}$ as a function of position and time. The orientation of the galaxy, calculation of axis limits, and color scheme are the same as in Figure 5. The time of each snapshot is labeled in gigayears at the bottom right hand corner of each panel. Later outputs are omitted as they show no qualitative changes since $t = 6.0$ Gyr.

kiloparsec and corresponding increase in $1 < r_{gc} < 3$ kpc persists until $t = 8$ Gyr (Figure 8, left panel). $S_{0.5,1,0}$ is born with more random vertical motion than $S_{0,0,0.5}$ initially had; like $S_{0,0,0.5}$, $S_{0.5,1,0}$ also experiences an early, dramatic increase in its vertical energy (Figure 8, right panel). Like $S_{0,0,0.5}$, $S_{0.5,1,0}$ shows almost no evolution of the vertical velocity dispersion after $t = 4$ Gyr. Only the central kiloparsec shows any appreciable change in the median height of the cohort after this time, with growth of the median height by about 100 pc (Figure 8, middle panel). $S_{0.5,1,0}$, like $S_{0,0,0.5}$, quickly becomes the kinematically hot, vertically extended population seen at redshift zero (Section 3). We also note that a central bulge-

like component with steeper density profile slope has already formed at early times as a result of bar-like instabilities in the early disk (see Guedes et al. 2012).

$t_{\text{form}} = [1.0, 2.0]$ Gyr The surface density distribution of $S_{1,0,2,0}$ is shown as a function of time in Figure 9. $S_{1,0,2,0}$ has a significant *in situ* population that forms either during or just prior to the merger event at $t = 2.0$ Gyr. This merger strongly impacts the cohort’s morphology. In spite of these turbulent beginnings, almost all of the $S_{1,0,2,0}$ stars have been assimilated into a coherent structure by $t = 4$ Gyr. $S_{1,0,2,0}$ ’s configuration is the first to show an ellipsoidal disk component; the disk is evident just after the cohort forms ($t = 2$ Gyr) and is obvious by $t = 4$ Gyr (see edge-on views). From $t = 4$ – 8 Gyr, the density distribution at $r_{gc} > 5$ kpc becomes more smooth, and any discernible tilt to the ellipsoid vanishes.

Despite differences in their assembly history, $S_{1,0,2,0}$ ’s kinematic properties are similar to those of older populations. The cohort’s radial surface density profile remains constant after $t = 4$ Gyr, except for some emigration away from the innermost kiloparsec (Figure 10, left panel). The initial, *in situ* population is born with relatively large σ_{v_z} , yet there is still a substantial increase in the random vertical motions of this cohort as its satellite-born populations merge (Figure 10, right panel), including the satellite still visible in the $t = 4$ Gyr snapshot. As with older cohorts, there is little heating at late times, and both the median σ_{v_z} and median height profiles show essentially no evolution after $t = 6$ Gyr.

$t_{\text{form}} = [3.0, 4.0]$ Gyr Many of the evolutionary trends established for stars with $t_{\text{form}} < 2$ Gyr are no longer evident when we examine $S_{3,0,4,0}$ (Figure 11). Here, the vast majority of the cohort is born *in situ* in the galactic disk; the early $S_{3,0,4,0}$ disk shows a prominent $m = 2$ mode spiral (top left of Figure 11). The initial snapshot also reveals two significant satellites that will soon interact with the *in situ* population. At $t = 5$ Gyr (top right), one of the two satellites is fully disrupted and the cohort’s strong spiral structure has dissipated. Over the next two billion years, the second satellite merges, the spiral structure dissolves, and there is a small but perceptible thickening of the disk. Stars at large radii continue to phase-mix over time ($t = 9$ Gyr, bottom right).

$S_{3,0,4,0}$ is the oldest cohort to have a dominant exponential component in its surface density radial profile (Figure 12, left

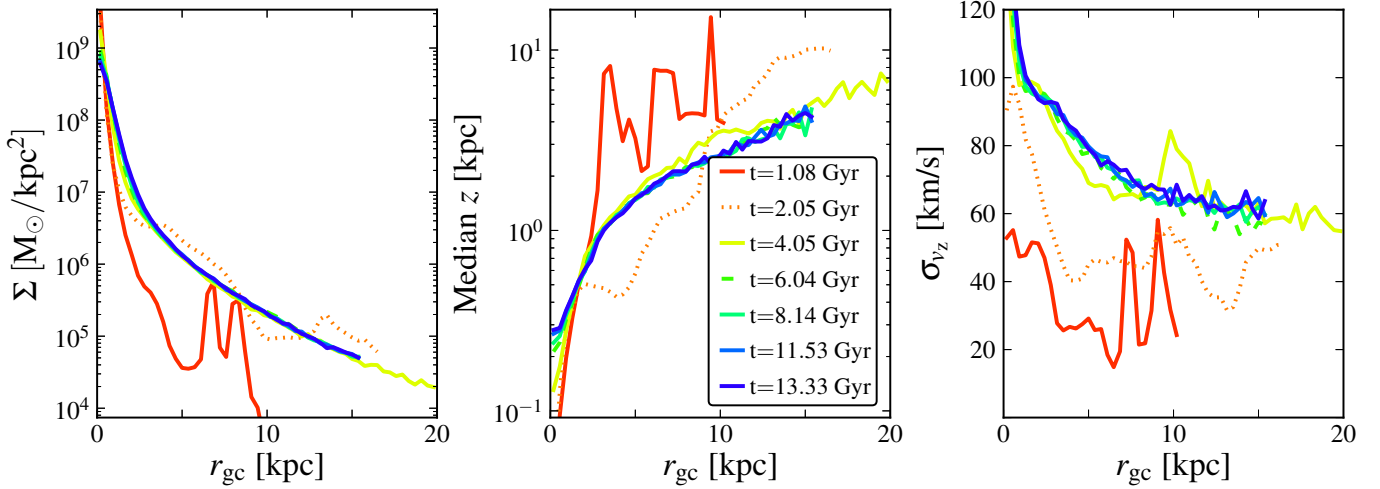


FIG. 8.— The radial profiles of surface mass density (left panel), median height above the disk plane (middle panel), and vertical velocity dispersion (right panel) for $S_{0.5,1.0}$ as a function of time. As in Figure 6, line color and type represent the age of the simulation when the profile was measured. The profiles now extend to $r_{gc} = 20$ kpc.

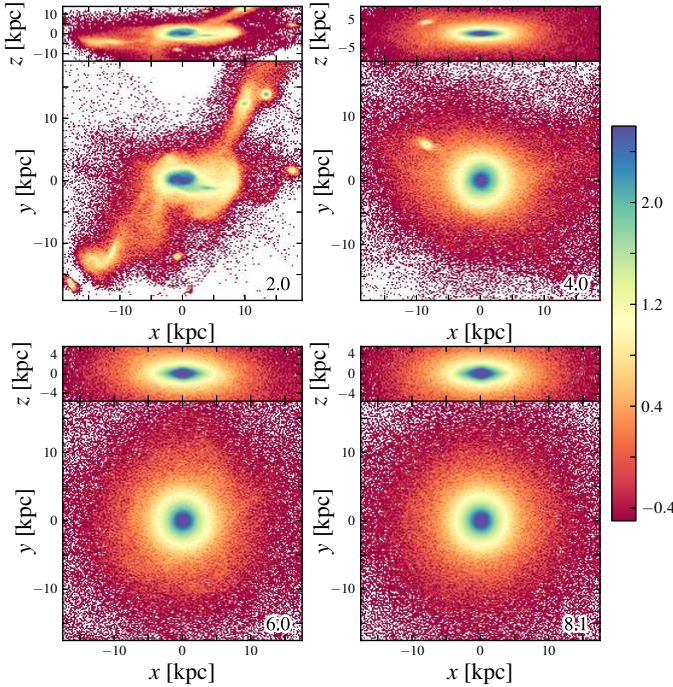


FIG. 9.— The surface density of $S_{1.0,2.0}$ as a function of position and time. The orientation of the galaxy, calculation of axis limits, and color scheme are the same as in Figure 5. The time of each snapshot is labeled in gigayears at the bottom right hand corner of each panel. Later outputs are omitted as they show no qualitative changes since $t = 8.1$ Gyr.

panel). As seen in the density plots, this cohort’s disk was in place at early times. The density profile shows some mass redistribution from the interior of the disk ($r_{gc} < 6$ kpc) to the outer disk over time, moderately increasing the cohort’s disk scale length. We investigate radial migration patterns of this cohort and others in Section 5. The radial profile of σ_{vz} (right panel) shows that $S_{3.0,4.0}$, while kinematically hot for a disk population, is born with lower internal energy than the older cohorts. $S_{3.0,4.0}$ members within $r_{gc} < 6$ kpc become modestly more energetic with time (Figure 12, right panel); over the last 10 Gyr, the population’s heating rate ($\Delta\sigma_{vz}/\Delta t$) is twice that of $S_{1.0,2.0}$. While the older populations became colder at increasing radius, $S_{3.0,4.0}$ has a positive σ_{vz} radial gradient;

we suspect that this is most likely due to relatively cold, disk orbits at smaller radii giving way to hotter halo kinematics past the break radius of the $S_{3.0,4.0}$ disk (Section 6 examines a kinematically selected disk sample). The median height of the cohort increases between $t = 4$ and $t = 5$ Gyr at $r_{gc} < 5$ kpc, while the outer disk settles to a thinner configuration.

$t_{form} = [7.0, 8.0]$ Gyr $S_{7.0,8.0}$ is illustrative of stellar populations born after redshift one: it forms almost exclusively in the disk and secularly evolves (Figure 13). The initial disk of $S_{7.0,8.0}$ is thin and shows obvious warping in its outskirts (Figure 13, top left panel). During this cohort’s evolution, a small bulge-like component re-grows in the central region of the galaxy (see Guedes et al. 2012), the initial outer disk warps weaken, and the cohort’s disk becomes more vertically and radially extended.

The cohort’s surface density radial profile clearly shows a central component giving way to an exponential disk at $r_{gc} \sim 2$ kpc (Figure 14, left panel). Like $S_{3.0,4.0}$, there is a net transfer of mass outwards; here, the effect is more dramatic and the donor region extends out to $r_{gc} \sim 11$ kpc. The inner disk ($r_{gc} \lesssim 10$ kpc), born cold, experiences significant vertical heating, with σ_{vz} at the solar radius growing from ≈ 20 km s $^{-1}$ to ≈ 30 km s $^{-1}$ (Figure 14, right panel). More cohort members populate the sparse outer disk, beyond $r_{gc} \approx 12$ kpc, over time and reduce the vertical velocity dispersion there. The central mass concentration seems distinct from the disk; stars in the central few hundred parsecs continue to move further from the plane throughout the cohort’s history. In a departure from previously examined cohorts, $S_{7.0,8.0}$ ’s entire disk slowly grows more vertically extended as a function of time (middle panel). The gradual increases in vertical velocity dispersion and median particle height are fractionally large compared to the late-time evolution of older cohorts, but they are still modest on an absolute scale.

5. RADIAL MIGRATION

Radial migration, i.e., stellar orbital angular momentum changes brought about by resonant interactions, can have a profound impact on the evolution of disk galaxies (Schönrich & Binney 2009a; Roškar et al. 2012a, and references therein). We now investigate the age cohorts’ migratory patterns. Stars are grouped into the same age cohorts used in Section 3, except that all stars with $t_{form} < 2$ Gyr are

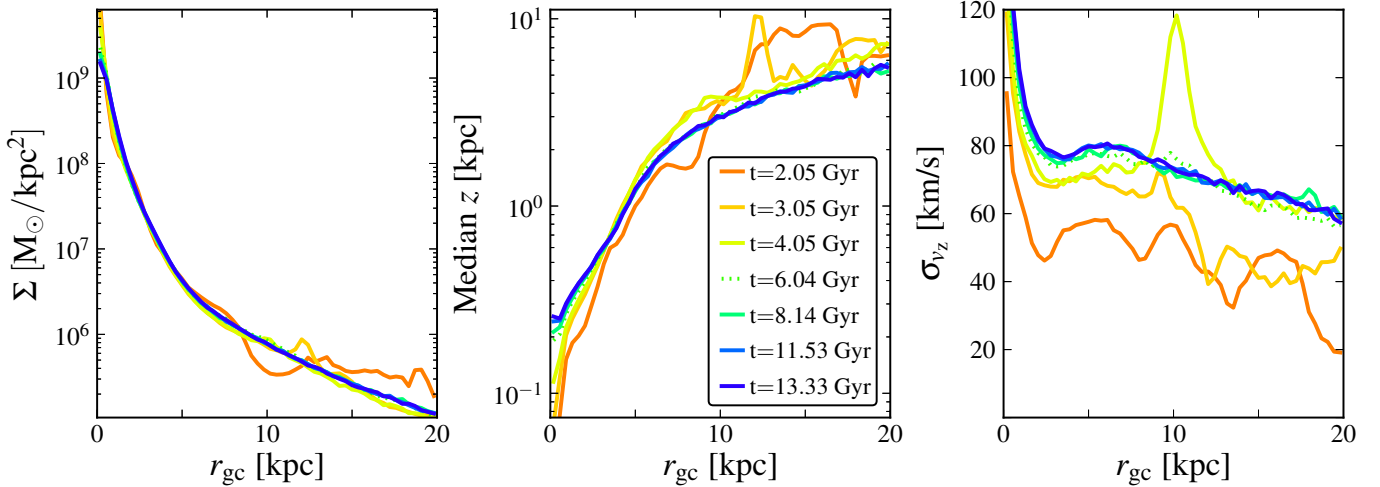


FIG. 10.— The radial profiles of surface mass density (left panel), median height above the disk plane (middle panel), and vertical velocity dispersion (right panel) for $S_{1,0,2,0}$ as a function of time. As in Figure 6, line color and type represent the age of the simulation when the profile was measured.

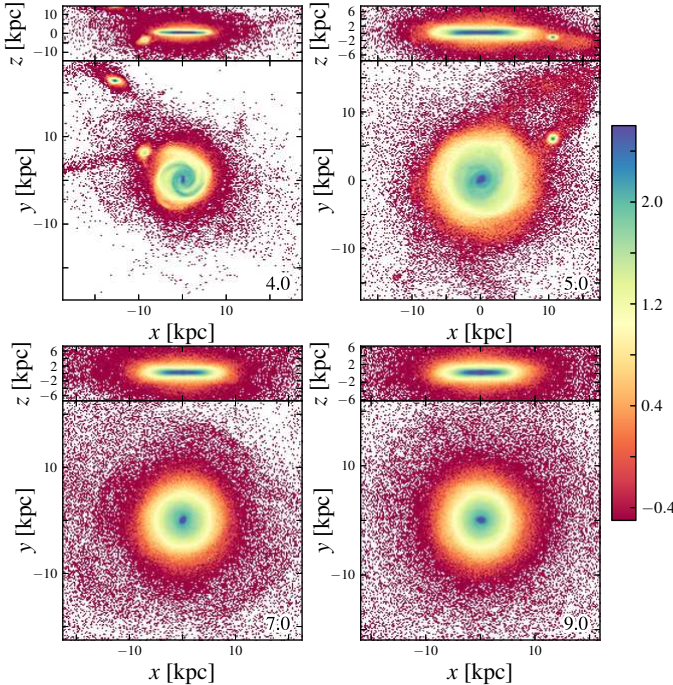


FIG. 11.— The surface density of $S_{3,0,4,0}$ as a function of position and time. The orientation of the galaxy, calculation of axis limits, and color scheme are the same as in Figure 5. The time of each snapshot is labeled in gigayears at the bottom right hand corner of each panel. Later outputs are omitted as they show no qualitative changes since $t = 9.0$ Gyr.

now labeled as a single cohort. We limit contamination from halo stars by constraining our migration analysis to particles within 4 kpc of the galactic plane at $z = 0$ ¹⁰.

Figure 15 shows the birth radii for cohort members currently residing in three different areas of the disk. The middle panel examines the present day solar annulus ($7 \leq r_{gc} \leq 9$ kpc). The oldest inhabitants of the solar annulus ($S_{0,0,0,2}$) come from the broadest range of formation sites. Stars born at large radii likely formed in a satellite halo before merging with the *in situ* population. Members of $S_{0,0,2,0}$ are predominantly associated with the spheroid (Section 3) and only

¹⁰ Relatively few particles have heights $z > 4$ kpc; our main results are independent of this selection cut.

contribute 7% of the total mass at this annulus (see Figure legend). For current solar annulus stars with $t_{form} > 2$ Gyr, progressively younger stars are less centrally concentrated at birth; the median r_{form} is 5.2, 6.6, 7.8, and 7.9 kpc for $S_{2,0,4,0}$, $S_{4,0,8,0}$, $S_{8,0,12,8}$, and $S_{12,8,13,4}$, respectively. Inside-out growth ensures that the same correlation between age and formation radius found in the solar annulus exists both in the inner (left panel) and outer (right panel) disk. Excluding $S_{0,0,2,0}$ and young stars with little time to migrate ($S_{12,8,13,4}$), the median radial excursion ($r_{final} - r_{form}$) of a cohort increases with cohort age and the final radius considered. Though the galaxy was built up in an inside-out fashion, it is important to note that the birth sites of old stars are not restricted to the central galaxy. For example, 20% of $S_{2,0,4,0}$ members currently in the solar annulus have $6 < r_{form} < 10$ kpc.

The radial excursions seen in Figure 15 are the result of two distinct scattering processes. Stars can be born on, or non-resonantly scattered to, eccentric orbits with large epicyclic amplitude, causing large in-plane motions that sweep through wide ranges in radius without increasing the orbit’s angular momentum. Stars can also gain or lose angular momentum, thereby changing their guiding centers, through resonant interactions¹¹ with spiral waves (e.g., Sellwood & Binney 2002; Roškar et al. 2012a), bar resonance overlap (Minchev & Famaey 2010), and satellite perturbations (Quillen et al. 2009; Bird et al. 2012). Figure 16 is similar to Figure 15 but it shows the distribution of current guiding center radii (R_g) for each age cohort; a star with angular momentum j_z has a guiding center equal to the radius of a circular orbit with the same angular momentum. If a star’s guiding center radius lies outside the indicated annulus, then the star appears in the annulus only because its eccentricity allows it to spend some of its orbit there. For example, the $S_{2,0,4,0}$ population in the solar annulus ($r_{gc} = 7.0 - 9.0$ kpc, yellow curve in the middle panel of Figure 16) are predominantly stars with $R_g < 6$ kpc, which are present near the solar radius because they are on the outer excursions of their eccentric orbits.

The trends with age in Figure 16 reflect the combination of inside-out formation and the age-kinematics correlation. Older cohorts have hotter kinematics either at birth or after

¹¹ Schönrich & Binney (2009a) refer to the latter process as “churning” and the former as “blurring.”

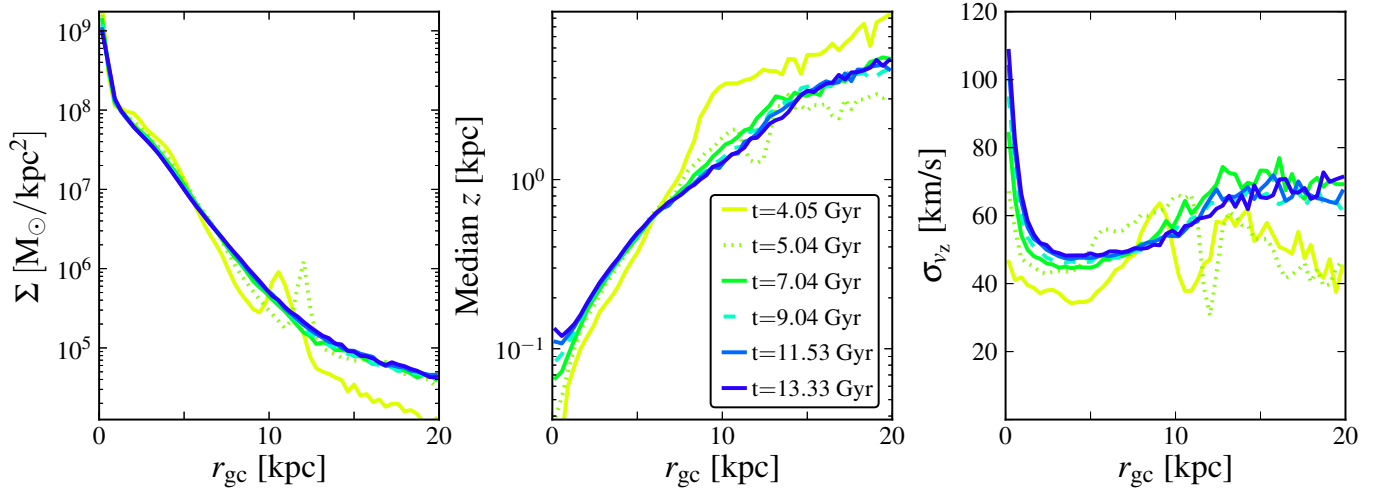


FIG. 12.— The radial profiles of surface mass density (left panel), median height above the disk plane (middle panel), and vertical velocity dispersion (right panel) for $S_{3.0,4.0}$ as a function of time. As in Figure 6, line color and type represent the age of the simulation when the profile was measured.

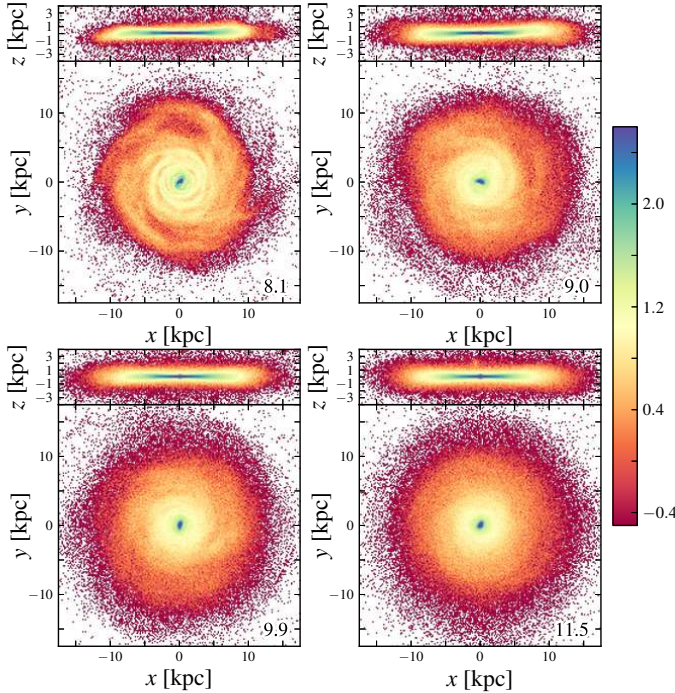


FIG. 13.— The surface density of $S_{7.0,8.0}$ as a function of position and time. The orientation of the galaxy, calculation of axis limits, and color scheme are the same as in Figure 5. The time of each snapshot is labeled in gigayears at the bottom right hand corner of each panel. Later outputs are omitted as they show no qualitative changes since $t = 11.5$ Gyr.

early heating by mergers, so they are more likely to spend time well outside their guiding center radius. Furthermore, because older stars form preferentially at small r_{gc} , the members of old cohorts found in outer annuli are primarily stars on outward radial excursions. By contrast, the young stars ($S_{12.8,13.4}$) in each annulus tend to be stars that were born in that annulus and have guiding centers in that annulus. The oldest stars ($S_{0.0,2.0}$) in each annulus are generally on highly eccentric, low angular momentum orbits with low R_g .

Scattering by the corotational resonances (CR) of spiral density waves is a particularly interesting mechanism of radial migration because it allows stars to shift their guiding centers (change angular momentum) without increasing orbital

eccentricity (Sellwood & Binney 2002). Figure 17 shows the distribution of ΔR_g , the change in guiding center radius between formation and $z = 0$, for the same three annuli illustrated in Figures 15 and 16. At $r_{gc} = 4.0\text{--}5.0$ kpc, these distributions are symmetric and fairly compact for all age cohorts. At the solar annulus, the $S_{2.0,4.0}$ and $S_{4.0,8.0}$ distributions are positively skewed and substantially broader, a trend that is still stronger at $r_{gc} = 11.0\text{--}12.0$ kpc. Even the $S_{8.0,12.8}$ cohort has a positively skewed ΔR_g distribution at this outer radius. The imposed condition of older stars at large radii preferentially selects stars that have experienced positive ΔR_g .

In sum, radial migration is an important effect in the outer galaxy. At the solar annulus and beyond, most stars with $t_{\text{form}} < 8.0$ Gyr formed well inside their current galactocentric radius (Figure 15). This migration reflects the combined impact of the higher orbital eccentricities in older populations, which allow stars to spend much of their orbits well beyond their guiding center radii (Figure 16), and angular momentum changes that shift guiding center radii outwards (Figure 17). The importance of radial migration in the outskirts of disk galaxies was made clear by Roškar et al. (2008b) and Sánchez-Blázquez et al. (2009); studies cite radial migration as the probable origin for the inverse age-radius gradients seen outside the break radius of nearby disk galaxies (e.g., Radburn-Smith et al. 2012; Yoachim et al. 2012). Our findings here, in conjunction with Figure 1, suggest that the older, migrating stars travel past the break radius of the galaxy’s gas reservoir at late times as traced by the density profile of the youngest stars ($S_{12.8,13.4}$). We discuss possible implications for thick disk evolution in the Section 6.

6. DISCUSSION

The shared lifetime of mono-age populations makes them physically intuitive descriptors of the galaxy formation process. A cohort’s members experience relatively similar dynamical histories. Their spatial origin tracks the star formation process, and their initial kinematics traces that of the gas at the cohort’s formation epoch. The oldest three cohorts ($S_{0.0,0.5}$, $S_{0.5,1.0}$, $S_{1.0,2.0}$) describe the galaxy’s turbulent youth. The first significant star formation occurs in the parent halo; the *in situ* component of the old cohorts show the classic signs of inside-out galaxy formation. As gas accumulates, cools, and collapses within the main halo, both the rate and radial extent of star formation contributing to the *in situ* population

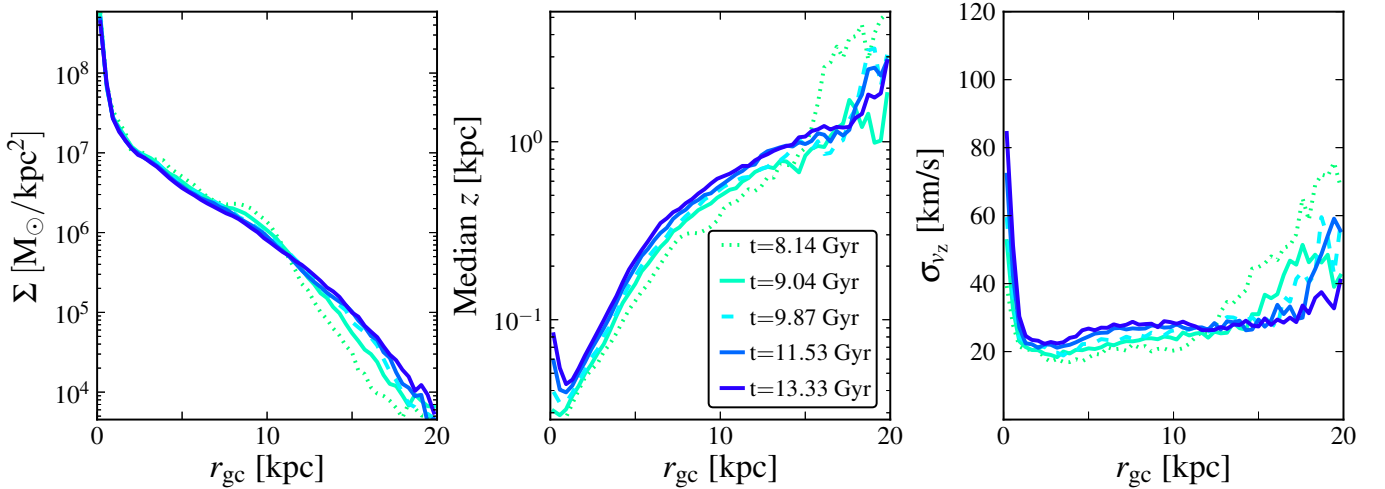


FIG. 14.— The radial profiles of surface mass density (left panel), median height above the disk plane (middle panel), and vertical velocity dispersion (right panel) for $S_{7.0,8.0}$ as a function of time. As in Figure 6, line color and type represent the age of the simulation when the profile was measured.

increases (Figures 5, 7, 9; top left panels). The spatial distribution of formation sites reveals a similar growth process for satellite-born stellar populations within their host halos (same Figures as above). During the major merger epoch, the energy in the velocity difference of the interacting satellite and parent halos is converted into the internal energy of the remnant (Binney & Tremaine 2008). All cohorts that exist at this time show dramatic and rapid increases in their internal energies (see kinematics of $S_{0.0,0.5}$, $S_{0.5,1.0}$, $S_{1.0,2.0}$; Figures 6, 8, 10). The present day spatial configuration and kinematic description of the aforementioned cohorts are in place once the last of their satellite-born members have merged with the parent halo ($t \approx 2$ -4 Gyr; see Figures 5 - 10). Almost 90% of stars with $t_{\text{form}} < 2$ Gyr are associated with the spheroid in the present-day galaxy (Table 1). The vast majority of stars born after $t = 2$ Gyr form in the disk (top left panel of Figures 11 and 13). Monotonic trends of position and velocity with age, consistent with stars forming from a cooling gas reservoir, characterize the disk’s assembly. $S_{3.0,4.0}$ and $S_{7.0,8.0}$ are illustrative examples; progressively younger cohorts form with larger radial break radii, colder vertical velocity distributions, and more compact vertical structure (see initial outputs in Figures 12 and 14). Younger cohorts are more susceptible to secular heating mechanisms (Section 4), but any changes in population thickness and velocity dispersion with time are not sufficient to disrupt the strong trends between cohort kinematics and age established by each cohort’s initial properties. The galaxy retains much of its assembly history: old cohorts are born thick (or quickly become so), while increasingly younger cohorts form thinner structures with longer radial scales. The galaxy forms inside-out and upside-down.

It is important to distinguish between a cohort’s internal energy at birth and subsequent evolution due to mergers or other scattering events. The former is wholly dependent on the properties of the gas when the cohort forms, while the latter is affected by gravitational interactions following the cohort’s inception. Figure 18 shows the ratio of mean rotational velocity to vertical velocity dispersion and median height for gas below the star formation threshold temperature of the simulation ($T < 3 \times 10^4$ K) and spatially coincident with the growing disk ($4 < r_{\text{gc}} < 8$ kpc, $|z| < 2$ kpc). Gas eligible to form stars becomes steadily more rotationally dominated as time progresses, leading to increasingly cooler, more vertically com-

pact stellar populations. Forbes et al. (2012) find similar results in one-dimensional models of the vertical structure of an evolving, star-forming disk. In our simulation, the star-forming gas rapidly contracts despite mergers and SNe feedback at $t < 3$ Gyr due to its high physical density (and short cooling time) within the small halo in the early universe. By $t \approx 3$ Gyr, the cooling time is long enough that strong perturbations by several mergers (Figures 7, 9, 11) and stirring by SN feedback (outflows are more powerful owing to higher star formation rates that peak at $t \approx 3.5$ Gyr) can prevent further collapse as suggested by the plateau at $t \approx 3$ -5 Gyr. After $t \approx 5$ Gyr, the merger rate declines rapidly, and the gaseous disk undergoes another period of collapse. The last minor merger, at $t \approx 7$ Gyr, may temporarily hinder further collapse, but the slow rate of contraction at $t > 8$ Gyr is more difficult to characterize. At present, the cold gas has $\sigma_{v_z} \approx 15$ km s^{-1} over the radial range ($0.5 < r_{\text{gc}} < 9$ kpc). The late-time evolution is the most uncertain regime of Figure 18, as it is most likely to depend on details of the SN feedback scheme and on poorly understood aspects of ISM physics that can influence the level of turbulent motion in the star-forming gas (see, e.g., Pilkington et al. 2011). The absence of molecular cooling in the simulation could artificially suppress vertical contraction at late times. However, the evolution at $t < 8$ Gyr reflects the dynamic assembly history of the galaxy and the impact of vigorous supernova feedback at early times, so we expect the trends to remain robust to details of the ISM modeling. The evolving kinematics of the parent gas component indicate that older stellar cohorts are truly born hotter than their younger counterparts, yielding a smooth transition from thick to thin disk over time.

In detail, the upside-down construction of the disk and the final stellar age-velocity relationship (AVR) are the integrated response of the age cohorts to the contracting gas disk and dynamical heating processes. In Figure 19, we show the temporal evolution of σ_{v_z} for a series of cohorts with 1-Gyr formation time bins. To compare with Figure 18, we further restrict our analysis to likely disk stars (see figure caption for selection criteria). The initial σ_{v_z} of each cohort closely follows the properties of the star-forming gas. The plateau seen in Figure 18 from $t \approx 3$ -5 Gyr is echoed by the similar initial σ_{v_z} of $S_{2.0,3.0}$, $S_{3.0,4.0}$, and $S_{4.0,5.0}$. Similarly, initial σ_{v_z} rapidly decreases from $S_{4.0,5.0}$ to $S_{6.0,7.0}$ as the gas reservoir contracts

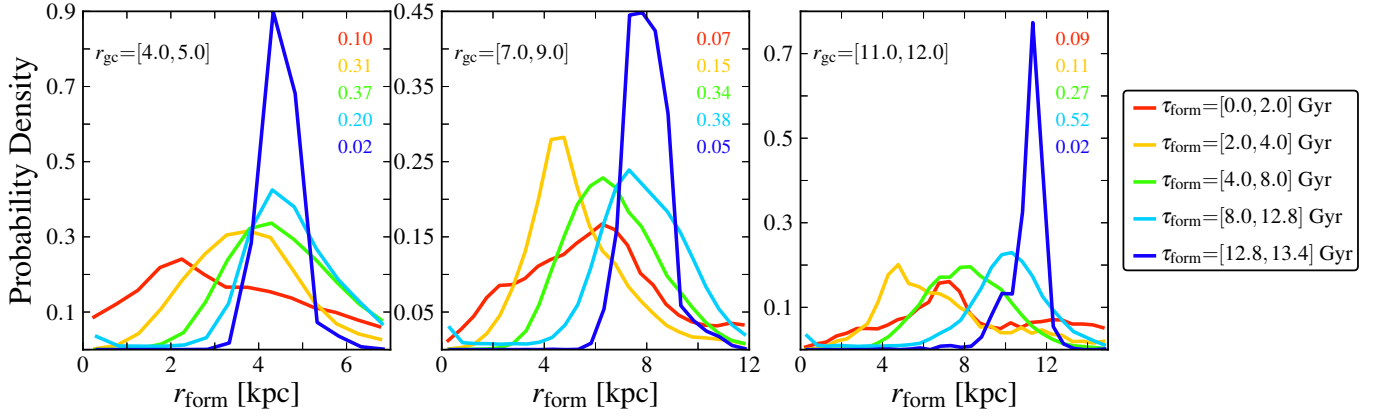


FIG. 15.— The distribution of formation radius for stars in different age cohorts residing at $r_{\text{gc}} = [4.0, 5.0]$, $r_{\text{gc}} = [7.0, 9.0]$, and $r_{\text{gc}} = [11.0, 12.0]$ at redshift zero (left to right, respectively). Color-coding differentiates the age cohorts and refers to their formation time (see legend). The fraction of mass within each annulus associated with each cohort is labeled with the corresponding color in the top right corner of each panel (listing is chronological by formation time).

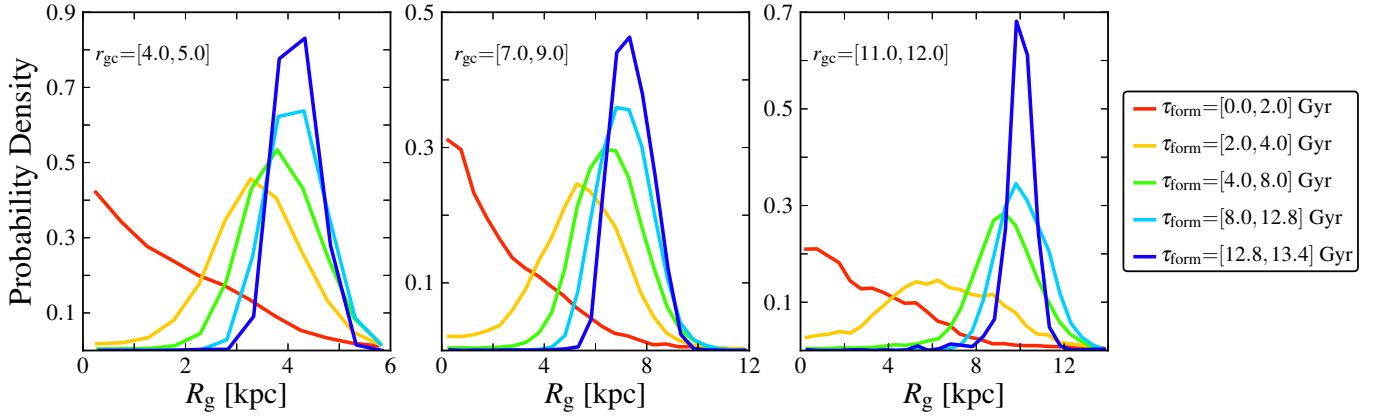


FIG. 16.— The current guiding center radius of age cohort members residing at $r_{\text{gc}} = [4.0, 5.0]$, $r_{\text{gc}} = [7.0, 9.0]$, and $r_{\text{gc}} = [11.0, 12.0]$ at redshift zero (left to right, respectively). Color-coding differentiates the age cohorts and refers to their formation time (see legend).

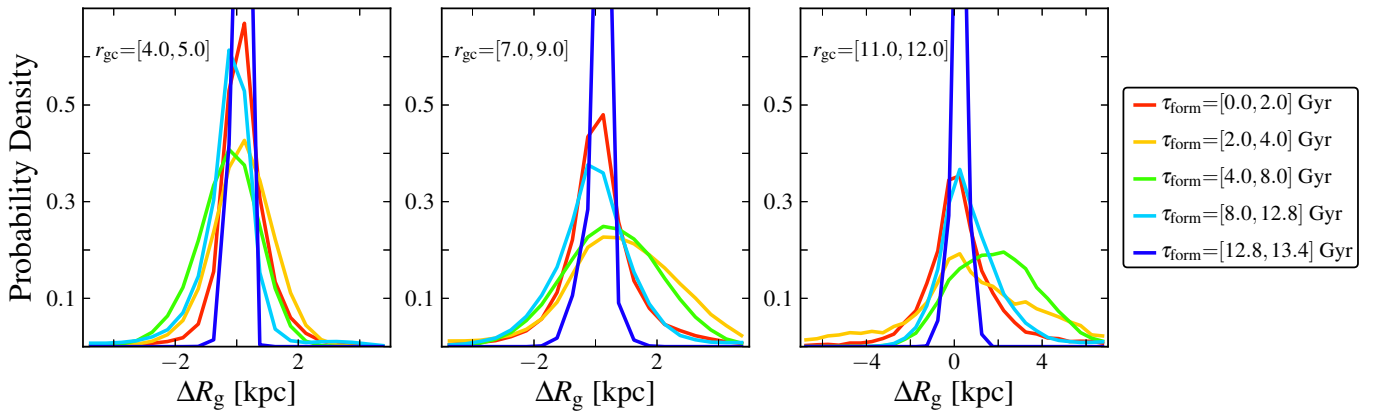


FIG. 17.— The change in guiding center radius of age cohort members residing at $r_{\text{gc}} = [4.0, 5.0]$, $r_{\text{gc}} = [7.0, 9.0]$, and $r_{\text{gc}} = [11.0, 12.0]$ at redshift zero (left to right, respectively). Color-coding differentiates the age cohorts and refers to their formation time (see legend). Positive ΔR_g indicates the particle has migrated outwards; particles migrating inwards have negative ΔR_g . Note the change of horizontal scale in the right panel.

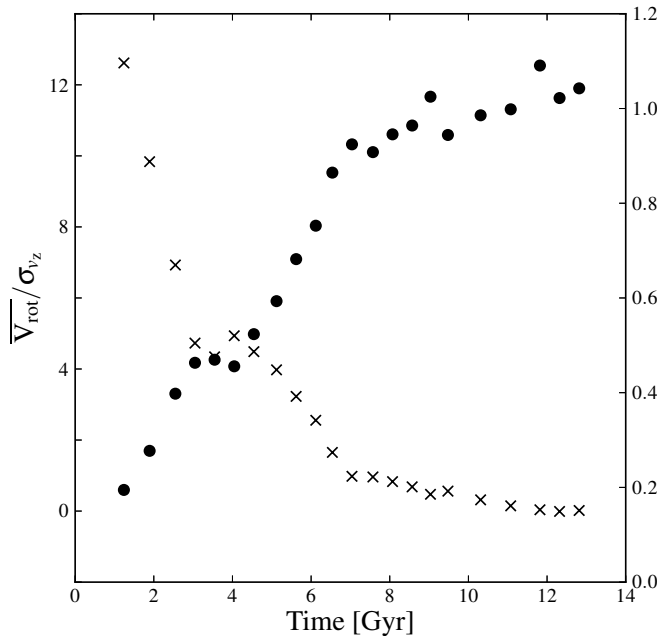


FIG. 18.— The ratio of mean rotational velocity to vertical velocity dispersion as a function of redshift for gas under the star formation threshold temperature of the simulation ($T < 3 \times 10^4$ K) in the disk and close to the plane ($4 < r_{\text{gc}} < 8$ kpc and $|z| < 2$ kpc, filled circles). The rotated crosses mark the corresponding median height of the cold gas reservoir. Gas viable for star formation becomes increasingly rotation-dominated and vertically compact throughout the simulation. To highlight trends over noise, each marker represents a three-point time-weighted moving average.

following the merger epoch, shows little change during the last minor merger (compare $\mathcal{S}_{6.0,7.0}$ and $\mathcal{S}_{7.0,8.0}$), and slowly declines thereafter. For all cohorts, the heating rate ($\delta\sigma_{v_z}/\delta t$, the slope of each line) measured over any one Gyr time interval (t_0, t_1) is anti-correlated with σ_{v_z} at t_0 , confirming that both mergers and secular scattering processes are more efficient heating mechanisms within colder stellar populations. Rapid increases in σ_{v_z} (> 5 km s $^{-1}$ Gyr $^{-1}$) are temporally coincident with merger activity, suggesting that the precise $z = 0$ stellar AVR may correlate with the galaxy’s accretion history. Secular heating does affect the AVR, increasing the dispersion of all cohorts over time, but it is clear from Figure 19 that the overall trend of σ_{v_z} with age is dominated by differences in initial dispersion at birth rather than by differential heating.

There is remarkable qualitative similarity between the age-kinematics trends measured in the $z = 0$ simulated galaxy and those observed in the MW. Cohort age is positively correlated with the population’s vertical extent but anti-correlated with its radial extent (Figure 1). Recent MW studies, using chemical composition as a proxy for stellar age, suggest similar structure in our own Galaxy (e.g., Bovy et al. 2012b). The alpha-enhanced, old, thick disk has a shorter scale length than the alpha-poor, young, thin disk (Cheng et al. 2012b). Stars far from the plane ($|z| > 1$ kpc) have similar [Fe/H] over a broad range in radius (Cheng et al. 2012a), suggesting that these stars may share a temporal origin. Stellar composition gradients in the vertical direction are even more well established; observations in the solar neighborhood and beyond find that $[\alpha/\text{Fe}]$ increases and [Fe/H] decreases with height above the disk plane (e.g., Bensby et al. 2003; Ruchti et al. 2010; Lee et al. 2011; Schlesinger et al. 2012). In addition to

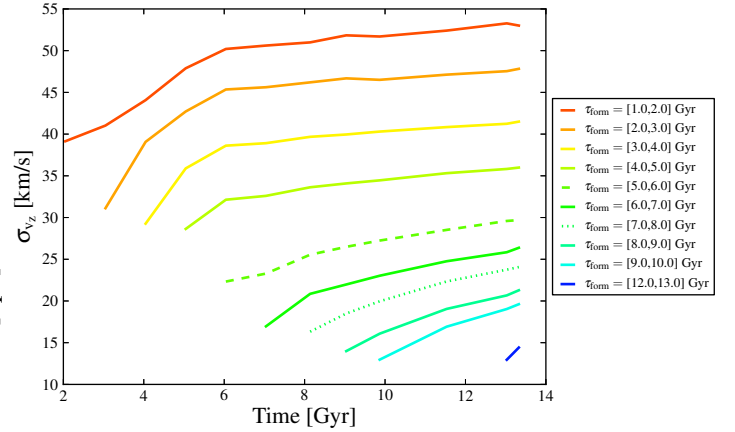


FIG. 19.— The temporal evolution of the vertical velocity dispersion for individual cohorts. For this figure, we select likely disk orbits ($\epsilon > 0.5$) that are spatially coincident with the disk ($4 < r_{\text{gc}} < 8$ kpc and $|z| < 2$ kpc) to directly compare with Figure 18. Color-coding differentiates the age cohorts and refers to their formation time; line types help distinguish amongst similar colors (see legend).

these geometrical differences, older cohorts in the simulated galaxy form with higher random motions¹² (Figure 4). This general age-velocity relationship (AVR) exists in the MW as well (e.g., Freeman 2008), and it is often explained by older stars having more time to be heated by various perturbing events (e.g., molecular clouds, transient waves, satellites). Here we find that while the disk-forming cohorts show a modest increase in their random motions with time, older cohorts *are born* kinematically hotter than younger stars. Our analysis of the mono-age populations makes it clear that the galaxy’s violent youth and *in situ* star-formation are responsible for the positively-sloped AVR, in addition to the age-density gradients present in both the radial and vertical dimensions.

The present-day age cohorts show near one to one correspondence with the mono-abundance populations of Bovy et al. (2012b,c), warranting a more direct comparison. As SEGUE’s G-dwarf sample primarily probes disk populations (Bovy et al. 2012b), we identify current disk members of the simulated galaxy and examine their kinematic properties as a function of age (Figure 20, see caption for selection criteria). Progressively older cohorts have shorter scale lengths (steeper slopes in left panel of Figure 20) and larger vertical extents (middle panel); both monotonic trends are remarkably smooth over the G-dwarf sample’s radial and presumed age range ($6 \leq r_{\text{gc}} \leq 12$ kpc and $\tau < 10$ Gyr, respectively). Bovy et al. (2012b) find that each MW mono-abundance population can be globally fit by a single exponential in the radial and vertical directions, but in the simulated galaxy each age cohort’s vertical density profile is itself a function of radius (Figure 20, middle panel). The observed mono-abundance populations show trends between vertical kinematics and age proxy: more alpha-rich, iron-poor populations have larger vertical velocity dispersions than their alpha-poor, iron-rich counterparts (Bovy et al. 2012c). The equivalent trend is found in the simulated galaxy, where progressively older cohorts have larger σ_{v_z} (Figure 20, right panel). Bovy et al. (2012c) find a shallow, but negative, radial gradient in σ_{v_z} for all mono-abundance populations. Both $\mathcal{S}_{2.0,4.0}$ and $\mathcal{S}_{4.0,8.0}$ show a decrease in σ_{v_z} with radius, but the vertical velocity dispersion of stars born in the last 5 Gyr ($\mathcal{S}_{8.0,12.8}$ and $\mathcal{S}_{12.8,13.4}$) slightly increases with radius. These results sug-

¹² The trend flattens for stars with $t_{\text{form}} < 2$ Gyr.

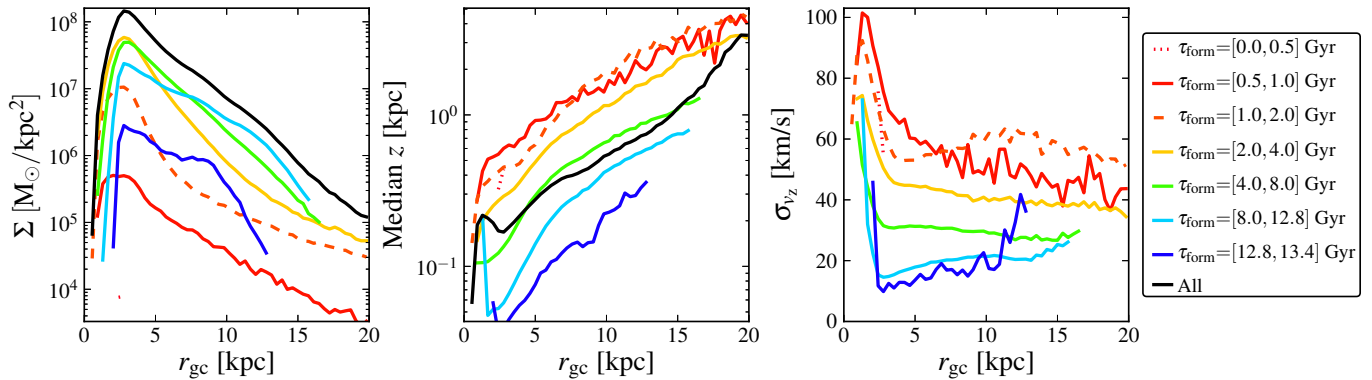


FIG. 20.— The present-day radial profiles of surface mass density (left panel), median height above the disk plane (middle panel), and vertical velocity dispersion (right panel) for all age cohort members selected to have orbits consistent with disk membership at redshift zero. Plotted members meet a circularity cut ($\epsilon > 0.5$) and have total energy greater than the median total energy of all stellar particles. The thick, black line is the total surface mass density (left panel) and median height (middle panel) of all selected stars. Color-coding differentiates the age cohorts and refers to their formation time; line types help distinguish amongst the oldest cohorts (see legend).

gest that age is a good proxy for chemical composition, a notion independently confirmed in a recent study (Stinson et al. 2013). Bovy et al. (2012a,b,c) favor internal, secular evolution mechanisms rather than discrete, external heating events to explain the smooth evolution of MW kinematic properties as a function of chemical abundance. Our simulated galaxy shows analogously smooth correlations of stellar kinematics with age, and the trends are largely imprinted at birth or immediately thereafter.

Thick disks are thought to be fundamental in understanding the balance of external and internal influences in disk galaxy formation (Section 1). Bovy et al. (2012a) showed that the mono-abundance populations span a continuous range of scale heights at the solar neighborhood and thereby argued that the MW does not have a distinct thick disk component. Rix & Bovy (2013) find that integrated vertical space density of all mono-abundance populations masquerades as observations classically identifying the thin and thick disk. At the solar annulus in the simulated galaxy, the vertical mass density profiles of individual age cohorts are progressively steeper for younger populations (Figure 3, middle panel). The superposition of all age cohorts in the solar annulus results in the familiar double-exponential profile observed in MW star counts (e.g., Gilmore & Reid 1983; Jurić et al. 2008). The two exponentially-fitted components are not distinct in origin; for example, the $\mathcal{S}_{2.0,4.0}$ and $\mathcal{S}_{4.0,8.0}$ cohorts populate both the thin and thick components at the solar annulus and vary their fractional contributions to these structures as a function of radius (Figure 3). Overall, our simulation leads to a “continuous” view of the thick disk similar to that advocated by Bovy et al. (2012a). We note that radial migration can produce a similar vertical structure (Schönrich & Binney 2009b), but in our simulation the double-exponential emerges principally from the superposition of trends imprinted by upside-down and inside-out formation.

The mechanisms primarily responsible for the main components of galactic structure (determined by kinematic decomposition, Table 1) can be inferred from the histories of corresponding member cohorts. The pseudobulge, predominantly made of stars with $t_{\text{form}} < 4$ Gyr, formed *in situ* and at early times (Figures 7 and 9; for a full investigation of bulge formation in a similar cosmological simulation, see Guedes et al. 2012). Over half the mass in the spheroid was born just prior to or during the major merger epoch ($t = 0.5\text{--}2.0$ Gyr), and another 25% formed immediately thereafter ($\mathcal{S}_{2.0,4.0}$), sug-

gesting stellar halo formation by stars scattered during the merger epoch, with a moderate contribution of stars stripped from satellites. The kinematically defined thick disk begins to form just before the end of the major merger epoch ($\mathcal{S}_{1.0,2.0}$ accounts for 25% of the thick disk’s mass at $z = 0$). Still, the majority of the thick disk forms in the parent halo after the merger epoch ends; over half the thick disk’s mass is in $\mathcal{S}_{2.0,4.0}$, which has a strong *in situ* component (Figure 12). MW observations may call for a significant contribution of $t_{\text{form}} = 4\text{--}6$ Gyr stars in a chemically defined thick disk (Bensby et al. 2004), and in our simulation such stars are formed overwhelmingly in the parent halo. Even as thick disk formation is well underway, stars with thin disk kinematics begin to appear. 26% of the stars on cold, thin disk orbits at $z = 0$ are members of $\mathcal{S}_{2.0,4.0}$, but many of these stars would likely be members of a chemically defined thick disk. The fraction of new stars that are kinematically associated with the thin disk increases with time in all subsequently formed cohorts.

Kinematic vs. chemical definitions of disk components likely involve significant mixing of the thin and thick populations (e.g., Navarro et al. 2011; Lee et al. 2011). However, our kinematics-based results are broadly consistent with the chemistry-based results of Brook et al. (2012), who study a cosmological zoom-in simulation of a disk galaxy that is $< 1/5$ the virial mass of the MW. They investigate the history of the gas reservoirs eventually forming the chemically-selected thin disk, thick disk and halo to describe galactic component formation in the annulus $r_{\text{gc}} = 7\text{--}8$ kpc. Their halo stars predominantly form *in situ* and are scattered to the halo during an early merger epoch, with a smaller fraction directly accreted from satellite galaxies. After the major merger epoch in their simulation ends, half of the thick disk forms from hot gas that was already in the central galaxy during the merger epoch. Brook et al. (2012) report a smooth transition in star formation from thick to thin disk stars, with the majority of their thin disk stars forming from smoothly accreted gas after the merger epoch. Brook et al. (2012) also find that old stars must move away from their formation radii to populate the solar vicinity. Our analysis in §5 leads to a similar conclusion and differentiates between kinematically hot orbits and guiding center changes (discussed further below). Our simulated galaxy and that of Brook et al. (2012) form their disk components in qualitatively similar fashions despite nearly an order-of-magnitude difference in galaxy mass and many dif-

ferences of detail in the simulations. Both experiments have relatively quiescent merger histories¹³ by construction, so we cannot say whether more active merger histories would substantially change the picture and/or lead to disagreement with observed MW structure.

Stars radially migrate throughout our simulation, and the redistribution of these stars impacts the galaxy’s construction to an extent. For simplicity, we focus on the role of radial migration in the creation of the thick disk at the solar annulus, which has been a topic of debate in the recent literature (e.g., Schönrich & Binney 2009a; Sales et al. 2009; Loebman et al. 2011; Brook et al. 2012; Minchev et al. 2012a; Roškar et al. 2012b). The basic idea is that the hotter populations of the inner galaxy will increase their scale heights as they move to the weaker vertical potential of the outer disk, but there are complications because of adiabatic cooling and dynamical selection of the stars that migrate. We now compare the kinematics of outwardly migrating ($\Delta R_g > 1.0$ kpc, designated “om”) and non-migrating ($|\Delta R_g| < 0.5$ kpc, “non”) disk populations¹⁴ in the solar annulus. When all disk stars currently residing at $7 < r_{gc} < 9$ kpc are considered, outwardly migrating stars and non-migrators have virtually the same vertical velocity dispersion ($\sigma_{v_z,om} = 29.7$ km s⁻¹ vs. $\sigma_{v_z,non} = 29.5$ km s⁻¹). These results are consistent with those of Minchev et al. (2012a), who find that outwardly migrating stars regulate themselves such that they are only marginally (< 5% level) hotter than the stellar populations at their destination radius, suggesting that migrators do not “thicken” the disk. A more complex picture emerges when we further dissect the sample and examine two older, thick-disk contributing cohorts ($S_{2.0,4.0}$ and $S_{4.0,6.0}$). In $S_{2.0,4.0}$, non-migrators have more vertical energy ($\sigma_{v_z,non} = 46.6$ km s⁻¹) than their outwardly migrating counterparts ($\sigma_{v_z,om} = 37.0$ km s⁻¹). $S_{4.0,6.0}$ shows the same relationship between migration and approximate vertical energy: non-migrators are hotter than outward migrators ($\sigma_{v_z,non} = 36.5$ km s⁻¹ and $\sigma_{v_z,om} = 29.1$ km s⁻¹, respectively).

The relationship between horizontal and vertical motions in an orbit is well-described using vertical action (J_z) invariance (e.g. Binney 2010; Binney & McMillan 2011; Schönrich & Binney 2012), and simulations show that migrating populations conserve their vertical action on average (Solway et al. 2012). Within an idealized, one-dimensional disk galaxy, the vertical velocity dispersion of an outwardly migrating population with constant J_z scales with the surface density of the disk, i.e., $\sigma_{v_z,om} \propto \Sigma^{1/4}$ (assuming $\Sigma \propto e^{-r_{gc}/r_d}$ where r_d is the scale length of the disk; see Minchev et al. (2012a) or Roškar et al. (2012b) for derivation in the 1D case, Schönrich & Binney (2012) for a more general treatment). In the same model galaxy, the vertical velocity dispersion of an isothermal, non-migrating population also scales with disk surface density but has an additional dependence on the scale height of the population as a function of radius (h_z), i.e., $\sigma_{v_z,non} \propto \sqrt{\Sigma h_z}$ (e.g., van der Kruit & Freeman 2011). Comparing the radial dependence of σ_{v_z} for migrating and non-migrating populations, we find

$$\frac{\sigma_{v_z,om}}{\sigma_{v_z,non}} \propto \frac{\Sigma^{1/4}}{\sqrt{\Sigma h_z}} \quad (2)$$

. This 1D scaling relationship cannot be used to make quan-

titative predictions of $\sigma_{v_z,om}/\sigma_{v_z,non}$, but it suggests that non-migrating stars are likely to have more vertical energy than outward migrators at a given radius when the disk scale length is short or h_z is a strong, positively-sloped function of radius. The simulated galaxy presents a more complicated, multi-component scenario, but our measurements within the solar annulus disk sample (previous paragraph) follow the relationships established in equation 2. There, $\sigma_{v_z,non}$ and $\sigma_{v_z,om}$ are nearly the same for the ensemble population, but $\sigma_{v_z,om}/\sigma_{v_z,non}$ decreases for $S_{2.0,4.0}$ and $S_{4.0,6.0}$, both of which have relatively short scale lengths and steep h_z ¹⁵ (Figure 20).

The trend of scale height with radius may therefore play an important role in the relative influence of migrators and non-migrators at large scale heights in MW-like galaxies. The simulated disk sample shows increasing median height (z_{med}) with radius as $\frac{\Delta z_{med}}{\Delta r_{gc}} = 0.07$ over the radial range $5 < r_{gc} < 14$ kpc (71 pc per kpc; middle panel, black line, Figure 20). Radial migration may contribute to this radially increasing scale height. We find that migrating stellar populations become more vertically extended as they move outward from the inner disk (in agreement with Roškar et al. 2012b), and some old, migratory groups currently have velocity dispersions exceeding the typical dispersion of thick disk stars in the MW ($\sigma_{v_z} = 35$ km s⁻¹, Bensby et al. 2003). These old stars populate both the traditional thin and thick disk components at their destination radius, so they are important when discussing population demographics and chemodynamic trends. The radial dependence of h_z observed here is contrary to the traditional notion of constant scale height in disk galaxies (e.g., van der Kruit & Searle 1982), but radially increasing stellar scale heights have been found in more recent measurements of a large sample of nearby disk galaxies (de Grijs & Peletier 1997, ; $\frac{\Delta h_z}{\Delta r_{gc}} = 0.05$ for MW Hubble type) and in the MW itself (Narayan & Jog 2002, ; $\frac{\Delta h_z}{\Delta r_{gc}} = 0.02$). Simulation improvements, including incorporating missing ISM physics such as molecular cooling, will likely flatten h_z and decrease the tension between simulations and observations. Individual age cohorts may still show steep h_z within the disk because of heating events like mergers, as even minor perturbations can cause flaring due to the low restorative force in the outer disk (e.g., Kazantzidis et al. 2008; Bournaud et al. 2009). Old, thick disk contributing cohorts (e.g., $S_{2.0,6.0}$) in MW-sized halos are particularly susceptible to flaring: these stars are typically born during a significant merger period (Section 4) and non-migrators at the solar annulus would form at the edge of a young, relatively compact disk. If this scenario is generic to older age cohorts in M_* halos, the maximal vertical extent of the thick disk (and similar structures in external galaxies) is likely set by the initially hot, *in situ* stars, as measured in the simulated galaxy.

7. CONCLUSIONS

We have investigated the structure, kinematics, and evolutionary history of stellar age cohorts in one of the highest resolution cosmological simulations ever run of the formation of a MW-like galaxy. This simulation produces good (though not perfect) agreement with many observed properties of the MW and similar galaxies (Guedes et al. 2011), so it may provide useful guidance to the origin of trends found in the

¹³ The last major merger in Brook et al. (2012) occurs at $z = 2.7$.

¹⁴ Disk stars are identified according to the criteria used for Figure 20.

¹⁵ The slope of h_z and the median height as a function of radius are equal if the vertical density distribution is exponential.

MW. We find remarkably good qualitative agreement between the trends for our mono-age cohorts and the observed trends for mono-abundance stellar populations in the MW found by Bovy et al. (2012a,b,c). Within the disk, older cohorts have shorter radial scale lengths, larger vertical scale heights, and hotter kinematics. The trends with age are smooth, but at a given radius the superposition of old, vertically-extended populations and young, vertically-compact populations gives rise to a total vertical profile that has the double-exponential form usually taken to represent the superposition of “thin” and “thick” disks in the MW.

Tracing back the formation history of each age cohort, we find that these present-day trends of spatial structure and kinematics are largely imprinted at birth. The oldest stars ($\mathcal{S}_{0.0,0.5}$, $\mathcal{S}_{0.5,1.0}$, and, to a lesser extent, $\mathcal{S}_{1.0,2.0}$) form during the active merging phase of the galaxy’s assembly, and these mergers scatter stars into rounded configurations and kinematically hot orbits, with the oldest stars being the most centrally concentrated. Even in these early cohorts, the great majority of stars form in the main halo rather than satellites, and phase-mixing erases differences in their distributions in any case. Younger cohorts form in disk-like configurations that are progressively more extended, thinner, and colder as t_{form} increases. The larger scale heights at earlier times are mostly inherited from the star-forming gas disk, which has a greater degree of turbulent support relative to rotational support (Figure 18), presumably because of stronger SN feedback from more vigorous star formation and more dynamical stirring by mergers and halo substructure. A disk cohort typically shows additional heating for another 1–2 Gyr after t_{form} , but thereafter the growth of velocity dispersion or vertical thickness is minimal.

The “inside-out” radial growth of the disk is a long-standing theoretical expectation — even if the gas disk were fully present at $t = 0$, star-formation would proceed more rapidly in the higher surface density, central regions. The resulting shape of the radial abundance gradient early in a galaxy’s evolution can therefore directly constrain feedback models (Pilkington et al. 2012; Gibson et al. 2013). At redshift zero, inside-out growth readily explains the direction of radial abundance gradients measured both locally and in external disk galaxies and is a central component of many Galactic chemical evolution models (e.g. Chiappini et al. 1997; Prantzos & Boissier 2000). Radial migration of stars is also an important ingredient in understanding chemical evolution (Wielen et al. 1996; Sellwood & Binney 2002; Roškar et al. 2008a; Schönrich & Binney 2009a), and it arises naturally in our simulation. In the outer disk, progressively older stars have progressively smaller formation radii on average, though the distribution of r_{form} is usually broad and includes some old stars born at large radius. The appearance of old stars at $r_{\text{gc}} > r_{\text{form}}$ is partly a consequence of increases in angular momentum (and thus guiding center radius) and partly a consequence of the larger orbital eccentricities of older stellar populations.

The “upside-down” evolution that we find for the disk’s vertical structure in our simulation is more novel, and it highlights a view of the MW’s thick disk that has growing support from analytic and numerical galaxy formation studies. In our simulation, the thick disk arises from continuous trends between stellar age and the evolving structure of the star-forming disk, not from a discrete merger event or from secular heating or radial migration after formation. The simulation clearly reproduces the basic phenomenology of the MW’s

thin and thick disks: a double-exponential vertical profile, and an increasing fraction of old stars at large distance from the plane and/or large random velocity. Forbes et al. (2012) have proposed a similar model for the origin of the thin/thick transition, based on one-dimensional simulations that track the evolution of turbulence in the star-forming gas. “Upside-down” formation is also observed to varying degrees in gas-rich merger simulations (Brook et al. 2004), zoom-in cosmological simulations (Stinson et al. 2013), and in clumpy, unstable gas-rich disks (Bournaud et al. 2009). The disk heating study of House et al. (2011) found, much like our study, that upside-down formation can naturally lead to a smooth stellar AVR at redshift zero. Quantitative tests of the simulation predictions will require using chemistry in place of age and carefully matching the selection criteria and measurement uncertainties of observational samples, a task that we reserve to future work.

Any simulation of galaxy formation has numerical limitations and physical uncertainties associated with the treatment of star formation and feedback. The specifics of our star formation treatment may matter for some of our conclusions, as we find that the thickness of the stellar disk is largely inherited from that of the star-forming gas. The Eris simulations have many successes in reproducing disk galaxy properties at high redshift (Shen et al. 2012) and low redshift (Guedes et al. 2011), but the adopted star formation model may predict galaxies that are too luminous for their halo mass relative to abundance matching constraints (Moster et al. 2013; Munshi et al. 2013). Solving this problem may require simulations with more vigorous feedback, and it will be important to confirm that the trends found here persist in such simulations. Furthermore, this simulation is a single realization selected to have a quiescent merger history, which limits our ability to draw statistical conclusions. However, we find good qualitative agreement with the simulation of Brook et al. (2012) despite a roughly order-of-magnitude difference in galaxy mass, which suggests that our conclusions are fairly robust, and upside-down formation also arises in the one-dimensional calculations of Forbes et al. (2012) as well as a small but diverse set of numerical experiments (e.g. Brook et al. 2004; Bournaud et al. 2009; House et al. 2011; Stinson et al. 2013). The good agreement between the properties of mono-age populations and observed trends in the MW further suggests that this recipe for galaxy formation has most of the right ingredients.

ELS envisioned a monolithic collapse of the proto-Galaxy, a scenario at odds with the hierarchical formation predicted in the CDM model. Our simulated galaxy forms self-consistently via violent, hierarchical accretion and cold flows at early times (Shen et al. 2012) followed by a nearly quiescent phase in which the disk grows predominantly from cold flow accretion and, to a lesser extent, from cooling of a diffuse warm/hot corona (Brooks et al. 2009; Guedes et al. 2011). Nonetheless, there are some qualitative similarities between our simulation results and the ELS scenario: the bulge (Guedes et al. 2012) and the thin and thick disks (this paper) form the overwhelming majority of their stars *in situ*, and these stars form in progressively more flattened, more rotationally supported configurations. The global distributions and correlations of galaxy properties — luminosities, colors, rotation speeds, morphologies, etc. — provide critical tests of galaxy formation simulations in the Λ CDM cosmology. As the realism and resolution of simulations continues to improve, and as chemodynamical surveys of the MW grow in

scope and detail, the close-to-home tests of simulation predictions against the observed correlations of the age, composition, spatial structure, and kinematics of stellar populations will provide steadily more powerful constraints on the theory of galaxy formation.

We thank Ralph Schönrich and the referee, Brad Gibson, for detailed comments on the original manuscript that led to significant improvements in the paper. We acknowledge fruitful conversations with Tom Quinn. We made use of pynbody (<http://code.google.com/p/pynbody>) in our analysis for this paper. J.B. acknowledges the support of the Vanderbilt Of-

fice of the Provost through the Vanderbilt Initiative in Data-intensive Astrophysics (VIDA) and the Distinguished University Fellowship awarded by the Ohio State University. S.K. is supported by the Center for Cosmology and Astro-Particle Physics at The Ohio State University. This research was partially funded by the Marie Curie Actions for People CO-FUND Program through the ETH Zurich Postdoctoral Fellowship awarded to J.G. Support for this work was provided by the NSF through grants AST-0908910, AST-1009505, AST-1211853, and OIA-1124453, and by NASA through grant NNX12AF87G. We acknowledge the Ohio Supercomputer Center (<http://www.osc.edu>) for computing time.

REFERENCES

- Abadi, M. G., Navarro, J. F., Steinmetz, M., & Eke, V. R. 2003, *ApJ*, 597, 21
- Aumer, M., White, S., Naab, T., & Scannapieco, C. 2013, *ArXiv e-prints*
- Bate, M. R., & Burkert, A. 1997, *MNRAS*, 288, 1060
- Bensby, T., Feltzing, S., & Lundström, I. 2003, *A&A*, 410, 527
- . 2004, *A&A*, 421, 969
- Bensby, T., Feltzing, S., Lundström, I., & Ilyin, I. 2005, *A&A*, 433, 185
- Binney, J. 2010, *MNRAS*, 401, 2318
- Binney, J., & McMillan, P. 2011, *MNRAS*, 413, 1889
- Binney, J., & Tremaine, S. 2008, *Galactic Dynamics: Second Edition*, ed. J. Ostriker & D. Spergel (Princeton University Press)
- Bird, J. C., Kazantzidis, S., & Weinberg, D. H. 2012, *MNRAS*, 420, 913
- Bournaud, F., Elmegreen, B. G., & Martig, M. 2009, *ApJ*, 707, L1
- Bovy, J., Rix, H.-W., & Hogg, D. W. 2012a, *ApJ*, 751, 131
- Bovy, J., Rix, H.-W., Hogg, D. W., et al. 2012c, *ApJ*, 755, 115
- Bovy, J., Rix, H.-W., Liu, C., et al. 2012b, *ApJ*, 753, 148
- Brook, C. B., Kawata, D., Gibson, B. K., & Freeman, K. C. 2004, *ApJ*, 612, 894
- Brook, C. B., Stinson, G. S., Gibson, B. K., et al. 2012, *MNRAS*, 426, 690
- Brooks, A. M., Governato, F., Quinn, T., Brook, C. B., & Wadsley, J. 2009, *ApJ*, 694, 396
- Bullock, J. S., & Johnston, K. V. 2005, *ApJ*, 635, 931
- Bullock, J. S., Kravtsov, A. V., & Weinberg, D. H. 2001, *ApJ*, 548, 33
- Casagrande, L., Schönrich, R., Asplund, M., et al. 2011, *A&A*, 530, A138
- Cheng, J. Y., Rockosi, C. M., Morrison, H. L., et al. 2012a, *ApJ*, 746, 149
- . 2012b, *ApJ*, 752, 51
- Chiappini, C., Matteucci, F., & Gratton, R. 1997, *ApJ*, 477, 765
- Cole, S., Aragon-Salamanca, A., Frenk, C. S., Navarro, J. F., & Zepf, S. E. 1994, *MNRAS*, 271, 781
- de Grijs, R., & Peletier, R. F. 1997, *A&A*, 320, L21
- Debatista, V. P., Carollo, C. M., Mayer, L., & Moore, B. 2004, *ApJ*, 604, L93
- . 2005, *ApJ*, 628, 678
- Eggen, O. J., Lynden-Bell, D., & Sandage, A. R. 1962, *ApJ*, 136, 748
- Fall, S. M., & Efstathiou, G. 1980, *MNRAS*, 193, 189
- Forbes, J., Krumholz, M., & Burkert, A. 2012, *ApJ*, 754, 48
- Freeman, K. C. 2008, in *Astronomical Society of the Pacific Conference Series*, Vol. 396, *Formation and Evolution of Galaxy Disks*, ed. J. G. Funes & E. M. Corsini, 3
- Gibson, B. K., Pilkington, K., Brook, C. B., Stinson, G. S., & Bailin, J. 2013, *A&A*, in press
- Gilmore, G., & Reid, N. 1983, *MNRAS*, 202, 1025
- Governato, F., Willman, B., Mayer, L., et al. 2007, *MNRAS*, 374, 1479
- Guedes, J., Callegari, S., Madau, P., & Mayer, L. 2011, *ApJ*, 742, 76
- Guedes, J., Mayer, L., Carollo, M., & Madau, P. 2012, *ArXiv e-prints*
- Haardt, F., & Madau, P. 1996, *ApJ*, 461, 20
- Haywood, M. 2008, *MNRAS*, 388, 1175
- Holmberg, J., Nordström, B., & Andersen, J. 2007, *A&A*, 475, 519
- Hopkins, P. F., Bundy, K., Croton, D., et al. 2010, *ApJ*, 715, 202
- House, E. L., Brook, C. B., Gibson, B. K., et al. 2011, *MNRAS*, 415, 2652
- Jurić, M., et al. 2008, *ApJ*, 673, 864
- Katz, N. 1992, *ApJ*, 391, 502
- Kauffmann, G., White, S. D. M., & Guiderdoni, B. 1993, *MNRAS*, 264, 201
- Kazantzidis, S., Bullock, J. S., Zentner, A. R., Kravtsov, A. V., & Moustakas, L. A. 2008, *ApJ*, 688, 254
- Kazantzidis, S., Zentner, A. R., Kravtsov, A. V., Bullock, J. S., & Debatista, V. P. 2009, *ApJ*, 700, 1896
- Kroupa, P., Tout, C. A., & Gilmore, G. 1993, *MNRAS*, 262, 545
- Lee, Y. S., Beers, T. C., An, D., et al. 2011, *ApJ*, 738, 187
- Loebman, S. R., Roškar, R., Debatista, V. P., et al. 2011, *ApJ*, 737, 8
- Mashchenko, S., Couchman, H. M. P., & Wadsley, J. 2006, *Nature*, 442, 539
- Matteucci, F., & Franco, P. 1989, *MNRAS*, 239, 885
- Mayer, L. 2012, in *Astronomical Society of the Pacific Conference Series*, Vol. 453, *Advances in Computational Astrophysics: Methods, Tools, and Outcome*, ed. R. Capuzzo-Dolcetta, M. Limongi, & A. Tornambè, 289
- McKee, C. F., & Ostriker, J. P. 1977, *ApJ*, 218, 148
- Minchev, I., Chiappini, C., & Martig, M. 2012b, *ArXiv e-prints*
- Minchev, I., & Famaey, B. 2010, *ApJ*, 722, 112
- Minchev, I., Famaey, B., Quillen, A. C., et al. 2012a, *A&A*, 548, A127
- Mo, H. J., Mao, S., & White, S. D. M. 1998, *MNRAS*, 295, 319
- Moore, B. P., Naab, T., & White, S. D. M. 2013, *MNRAS*, 428, 3121
- Munshi, F., Governato, F., Brooks, A. M., et al. 2013, *ApJ*, 766, 56
- Narayan, C. A., & Jog, C. J. 2002, *A&A*, 394, 89
- Navarro, J. F., Abadi, M. G., Venn, K. A., Freeman, K. C., & Anguiano, B. 2011, *MNRAS*, 412, 1203
- Navarro, J. F., & Steinmetz, M. 1997, *ApJ*, 478, 13
- Nemec, J., & Nemec, A. F. L. 1991, *PASP*, 103, 95
- Nemec, J. M., & Nemec, A. F. L. 1993, *AJ*, 105, 1455
- Pilkington, K., Gibson, B. K., Calura, F., et al. 2011, *MNRAS*, 417, 2891
- Pilkington, K., Few, C. G., Gibson, B. K., et al. 2012, *A&A*, 540, A56
- Prantzos, N., & Boissier, S. 2000, *MNRAS*, 313, 338
- Quillen, A. C., & Garnett, D. R. 2001, in *Astronomical Society of the Pacific Conference Series*, Vol. 230, *Galaxy Disks and Disk Galaxies*, ed. J. G. Funes & E. M. Corsini, 87–88
- Quillen, A. C., Minchev, I., Bland-Hawthorn, J., & Haywood, M. 2009, *MNRAS*, 397, 1599
- Radburn-Smith, D. J., Roškar, R., Debatista, V. P., et al. 2012, *ApJ*, 753, 138
- Rix, H.-W., & Bovy, J. 2013, *A&A Rev.*, 21, 61
- Roškar, R., Debatista, V. P., & Loebman, S. R. 2012b, *ArXiv e-prints*
- Roškar, R., Debatista, V. P., Quinn, T. R., Stinson, G. S., & Wadsley, J. 2008a, *ApJ*, 684, L79
- Roškar, R., Debatista, V. P., Quinn, T. R., & Wadsley, J. 2012a, *MNRAS*, 426, 2089
- Roškar, R., Debatista, V. P., Stinson, G. S., et al. 2008b, *ApJ*, 675, L65
- Ruchti, G. R., Fulbright, J. P., Wyse, R. F. G., et al. 2010, *ApJ*, 721, L92
- Sales, L. V., Helmi, A., Abadi, M. G., et al. 2009, *MNRAS*, 400, L61
- Sánchez-Blázquez, P., Courty, S., Gibson, B. K., & Brook, C. B. 2009, *MNRAS*, 398, 591
- Schlesinger, K. J., Johnson, J. A., Rockosi, C. M., et al. 2012, *ApJ*, 761, 160
- Schönrich, R., & Binney, J. 2009a, *MNRAS*, 396, 203
- . 2009b, *MNRAS*, 399, 1145
- . 2012, *MNRAS*, 419, 1546
- Searle, L., & Zinn, R. 1978, *ApJ*, 225, 357
- Sellwood, J. A., & Binney, J. J. 2002, *MNRAS*, 336, 785, (SB02)
- Shen, S., Madau, P., Aguirre, A., et al. 2012, *ApJ*, 760, 50
- Shen, S., Wadsley, J., & Stinson, G. 2010, *MNRAS*, 407, 1581
- Solway, M., Sellwood, J. A., & Schönrich, R. 2012, *MNRAS*, 422, 1363
- Soubiran, C., Bienaymé, O., Mishenina, T. V., & Kovtyukh, V. V. 2008, *A&A*, 480, 91
- Spergel, D. N., Bean, R., Doré, O., et al. 2007, *ApJS*, 170, 377
- Stinson, G., Seth, A., Katz, N., et al. 2006, *MNRAS*, 373, 1074
- Stinson, G. S., Bovy, J., Rix, H.-W., et al. 2013, *ArXiv e-prints*
- van der Kruit, P. C., & Freeman, K. C. 2011, *ARA&A*, 49, 301
- van der Kruit, P. C., & Searle, L. 1982, *A&A*, 110, 61
- Villalobos, Á., & Helmi, A. 2008, *MNRAS*, 391, 1806
- Wadsley, J. W., Stadel, J., & Quinn, T. 2004, *New Astronomy*, 9, 137
- White, S. D. M., & Frenk, C. S. 1991, *ApJ*, 379, 52
- White, S. D. M., & Rees, M. J. 1978, *MNRAS*, 183, 341
- Wielen, R. 1977, *A&A*, 60, 263

Wielen, R., Fuchs, B., & Dettbarn, C. 1996, A&A, 314, 438
Yanny, B., Rockosi, C., Newberg, H. J., et al. 2009, AJ, 137, 4377
Yoachim, P., & Dalcanton, J. J. 2008, ApJ, 682, 1004

Yoachim, P., Roškar, R., & Debattista, V. P. 2012, ApJ, 752, 97